A numerical and experimental study of a new Savonius wind rotor adaptation based on product design requirements

Jorge Manuel Mercado-Colmenero [a], Miguel Angel Rubio- Paramio [b], Francisca Guerrero-Villar [c], Cristina Martin-Doñate [d*]

[a , b, d] Department of Engineering Graphics Design and Projects. University of Jaen. Spain

[c] Department of Mechanical Engineering. University of Jaen. Spain

*Corresponding Author[d]

Campus Las Lagunillas, s/n. Building A3-210

23071 Jaen (Spain)

Phone: +34 953212821, Fax: +34 953212334

E-mail: jmercado@ujaen.es [a], marubio@ujaen.es [b], mgvillar@ujaen.es [c], cdonate@ujaen.es [d]

Abstract

This paper presents the numerical-experimental study carried out on a new rotor adapted from a Savonius rotor. Aesthetic, ergonomic and functional requirements have been incorporated into it in order to be part of sustainable consumer products. The new rotor consists of a parametric model adaptable to the dimensions and geometry of the products which it will be part of. A set of translation, symmetry, rotation and scaling operations have been applied to the bucket sections of the Savonius rotor by means of transforming the initial cylindrical buckets into topological surfaces with an organic shape. The new modified Savonius rotor and the conventional Savonius with the same Aspect Ratio have been tested in an open jet wind tunnel in order to verify the influence level of product design parameters on rotor performance, in terms of power coefficient, torque coefficient and mechanical power generated. Experimental tests have been carried out for Reynolds values in the range of [$3{,}430\cdot10^4$ and $1{,}419\cdot10^5$]. A numerical analysis using an incompressible unsteady Reynolds average Navier Stockes model has been validated by means of the experimental results. Experimental and numerical results coincide with a 3.5% error. The behavior of the turbine has been analyzed by varying the angle of rotation for the sections of its buckets. Using a rotation angle of 45 ° the power coefficient values improve by 32% compared to the values obtained using an angle of 0 °. The rotor has been dimensioned for its application in a patented consumer product of small dimensions and requirements of lateral accessibility to its interior. Under these limited conditions the rotor meets the small-scale energy requirements of the product. The new rotor is designed as an aid to the energy consumption of the product in which it is incorporated, maintaining the advantages of a conventional Savonius rotor as self-starting, easy manufacture and maintenance, obtaining at the same time a product that sells better, is more able to integrate into its environment and is customizable for the consumer.

Keywords: Savonius wind rotor, Rotor shape, CFD, Wind tunnel testing, Sustainable product development

1. Introduction

Industrial design is a differentiating factor of the product nowadays and a vital strategy tool for the companies, with the function of innovating and creating future markets. Consumers demand products that have little environmental impact, both in their manufacture and during use throughout their life cycle. This fact can become an advantage for a company that designs products that help reduce pollution levels, thus fulfilling the requirements of new generations of consumers. One of the main sources of environmental impact is the energy consumed by the products. Reviewing the design from the functional point of view, looking for opportunities in the reduction of the energy consumption or evaluating the way to generate energy consumption by means of a better geometry can present great advantages.

Wind energy is one of the renewable energy sources capable of generating clean energy economically [1] being a feasible alternative to reduce the dependency on conventional energy sources [2]. Wind energy has been adapted by industries and accommodated by individual users due to its availability, ease of maintenance and low cost operation [3]. In recent years, horizontal-axis turbines have focused research given their high level of aerodynamic efficiency [4], requiring complex design criteria [5]. In contrast, vertical axis turbines have other advantages such as their ability to generate power at relatively low wind speeds [6], simple installation and maintenance [7], ease of manufacture, and a low risk of damage to birds. Savonius rotors fall within the scope of vertical rotors characterized by generating a high starting torque in any wind direction even at low speed [8], being highly silent by operating at a very low tip speed ratio. As a particular advantage, they present a simple design of their buckets or buckets, a feature that allows the introduction of criteria of the aesthetic type in its geometry, being suitable for small scale applications.

Improving the performance of the Savonius rotor as well as obtaining the geometric parameters that provide adequate efficiency has focused the attention of a large number of researchers and designers in recent years. The work has focused mainly on evaluating a set of parameters related to the geometric surface of the buckets as well as their relative spacing, the overlap ratio and the number of turbine stages among other variables.

The surface of the buckets has a great influence on the performance of the rotor and therefore on the value of Power Coefficient C_p. The buckets of the Savonius turbine can have very varied forms depending on the geometry of the curves that make up their topology. In an effort to improve the performance of the Savonius rotor, several researchers have modified the surface of the buckets by evaluating their influence on rotor performance. Saha et al. [9] applied a geometric torsion operation to the three buckets of a Savonius rotor, validating their performance in a wind tunnel at low speed. The experimental results show the potential of the rotor with twisting buckets in terms of increased efficiency, self-starting capability and smoothness compared to those of a conventional Savonius rotor. Roy et al. [10] performed tests on a modified Savonius-style two-buckets turbine, comparing the results of C_p versus the results of other rotors such as a conventional Savonius rotor, a semi-elliptical section rotor, and two other Benesh and Bach type rotors. Their results show a gain of 34% in the maximum power coefficient compared to those obtained with the other designs. Kamoji et al. [11] carried out experimental studies with a modified Savonius rotor (Bach type) of one stage, with end plates, both with and without inner shaft. With an overlap ratio equal to 0, bucket arc angle of 124 ° and an aspect ratio of 0.7 the modified rotor has a maximum Power Coefficient C_p higher than that of a conventional Savonius rotor. Roy et al. [12] presented a transient analysis of the forces acting on a novel two-bladed Savonius style wind turbine. A significant performance improvement is achieved with the new design as compared to the conventional design due to its increased lift and moment arm contribution. More recently Tian et al. [13] introduced an optimization procedure of a Savonius wind rotor with different convex and concave sides to maximize the power efficiency.

Geometrically transforming the buckets by means of rotating operations allows the obtaining of helical Savonius turbines. Lee et al. [14] studied the variation in power coefficient and flow patterns of a Savonius turbine applying different rotation angles to its buckets and determined that the value of C_{pmax} corresponds to a design with rotation angle of 45 °. Damak et al. [15] proposed the use of a Savonius rotor with a rotation angle of 180º. In this design the rotor is obtained from the curve generated by a marker that moves vertically at constant speed over a rotating cylinder. The results obtained by the author indicate that an increase in the Reynolds and in the overlap ratio has a positive effect on the global features of the helical Savonius rotor. Yang et al. [16] carried out an experiment using a helical turbine in a wind tunnel. Their results indicated that an increase in rotation angle improved performance at low speed and reduced the net positive torque.

Another characteristic design parameter of the Savonius rotor geometry is the aspect ratio or ratio between the height H_S of the rotor and the diameter D_S of its buckets. The aspect ratio has an influence on the angular velocity of the rotor and on the torque that it generates, so that when the value of the aspect ratio is reduced the torque generated increases, and by increasing the torque generated the speed of rotation of the rotor also increases [17]. An increase in the aspect ratio may have a considerable influence on the power coefficient. However, it is not desirable to have high values of the aspect ratio due to the decrease in the power-to-weight ratio [18]. Blackwell et al. [19] showed that the efficiency increases slightly when the height/diameter ratio increases. Kamoji et al. [11] found the maximum value of C_p for a rotor with an aspect ratio of 0.7 and with a Savonius rotor design with modified buckets. Saha et al. [20] showed that aspect ratio values of around 4.0 appear to lead to the best power coefficient for the conventional Savonius rotor.

The overlap ratio is defined as the ratio of the overlap distance of the buckets to their D_S diameter. The Savonius rotors that include an overlap between their buckets present better features in their starting [18]. Akwa et al. [21] studied numerically the influence of the overlap ratio on a Savonius rotor. The results showed that the maximum performance appears in an overlap ratio of 0.15. Fujisawa et al. [22] also determined that the torque and the power output of the rotor reaches a maximum for an overlap of 0.15. Ushiyana et al. [23] showed that for buckets with semicircular sections the appropriate overlap ratio is 20 to 30%. Jian et al. [24] indicated in their study that the optimum overlap ratio is in a value of 0.167 for a single-stage rotor. There are many papers [18] regarding the study of the overlap ratio, establishing the optimal values of this parameter in the range of [0.15-0.25].

The number of buckets in the Savonius rotors is an effective parameter which influences the starting torque but at the same time can decrease the value of C_p. The reason is that the increase of the convex area of the buckets in a given position tends to reduce the torque difference of the concave sides, which eventually affects the value of C_p. Saha et al. [25] determined that the optimal number of buckets is 2 for a Savonius rotor either of 1, 2 or 3 stages. Ali et al. [26] conducted a comparative experimental study of a 2 and 3 bucket rotor, concluding that the rotor with two buckets is more efficient and has a higher power coefficient than the rotor with three buckets, with the same test conditions. Mahmoud et al. [27] tested rotors of 2, 3 and 4 buckets with different aspect ratios, and without overlap between the buckets. As a conclusion to their research, he determined that the rotor of two buckets for one and two stages and with different aspect ratios provided better performance than rotors with three and four.

The performance of the Savonius rotor can also be improved by introducing several Savonius rotors in different stages. A multi-stage rotor is characterized by having several rotors at different heights which incorporate an angular displacement between them. The most important improvement of introducing rotors in several stages is to generate a more uniform torque throughout the 360º. However, the fact of having rotors in several stages means that the value of C_p decreases. Jian et al. [24] obtained a level of decrease of power when using a rotor of two stages of 20% less than when using a single stage rotor. Hayashi et al. [28] designed a new three-stage rotor with a 120 ° phase-shift angle in order to decrease torque variation and improve starting features. Although the rotor they developed needs to make improvements in the aspect ratio at each stage, the three-stage rotor without guide has better torque features than the single-stage rotor with guides for a tip speed ratio greater than 0.8. Menet et al. [29] tested Savonius rotors in different stages, obtaining as a result that the coefficient of starting torque of the double-stage rotor is never negative, regardless of the direction of the wind, and never near to the value 0. In this way, the rotor starts after a period without wind. They also found good angular stability of the dynamic torque during rotor operation.

The addition of curtains in front of the rotor significantly improves its performance. The curtains are placed in order to reduce the negative torque caused by the return bucket and increase the power coefficient. Suitable angles for the curtains plates are $\alpha = 45°$ and $\beta = 15°$. Altan et al. [30] designed a curtains to improve the low level of efficiency of Savonius wind turbines. Their design avoids negative torque in the convex bucket of the rotor. In a later study [31] Altan et al. introduced a straight flap which reduces the effects of the compression of the flow within the bucket so that the rotor performance is increased. Based on such optimizations it achieves a power coefficient increase of about 20%. Mohamed et al. [32] positioned an obstacle to protect the return bucket of the Savonius turbine and better drive the orientation of the flow towards the advance bucket. In this way it obtains a considerable improvement of the performance of the Savonius turbines, with a relative increase in the power coefficient of more of 27%.The performance of a Savonius rotor can be improved using multiple quarter blades. Sharma et al.[33] added multiple quarter blades to conventional configuration, observing an improvement in the coefficient of power of 8.89% to 13.69 % for different inlet velocities over the conventional configuration. In a later study Sharma et al.[34] quantify the effect of layered multiple miniature blades on the coefficient of power of a Savonius rotor using simulation software, observing an improvement in COP spanning of between 8.1% and 11.34% with the modified configuration. Korprasertsak et al.[35] proposed an optimal design of wind boosters for vertical axis wind turbines at low speed. The wind booster comprises a number of guide vanes, which are mounted around a VAWT. The guide vanes direct wind to impact VAWT blades at effective angles while passages between each guide vane are arranged to accelerate wind. The guiding and throttling effects of the wind booster are able to increase angular speed, leading to an increase in the mechanical power of the VAWT.

The use of end plates in the design of the rotor also improves the performance of the Savonius rotor. Alexander et al. [36] studied the effect of the end plates on the performance of the Savonius rotor, obtaining a high power coefficient. To improve the performance of the rotor, a value of the diameter of the end plates 10% higher than the diameter of the buckets D_s, is recommended for a rotor with an aspect ratio of 1.0 [18].

Vertical axis turbines combine functional performance with a strong aesthetic component. The use of this kind of rotor allows the introduction of geometric requirements in its technical specifications which often have an important role in the placement of rotors inside protected areas [37]. Coastal and mountainous areas are optimal for the location of vertical rotors due to wind conditions, however these locations tend to be areas of a high visual impact which can make a poorly harmonic design not suitable for these locations. Vertical rotors have the advantage of operating in a turbulent mode and with low wind speed [38]. They are optimal for use in cities [39], urban areas [40], sub-urban and remote areas [41] since its installation is possible in the top of many buildings [42].Vertical axis wind turbines have the greatest future prospects among all wind technologies for small-scale power generation in the built environment [43]. In addition, the electrical production of the vertical rotors works in a distributed way, managing a large number of small renewable sources as if it were a single larger source, like a virtual power plant. These reasons make vertical rotors suitable for introduction into products for smart cities whose objective is to use resources efficiently, saving energy and improving the environmental footprint [44].

Working on the design of a rotor involves taking into account its appearance, but also incorporating this quality into the achievement of a good technical performance. Wind rotors and specifically vertical rotors are ideal components of consumer products because of their symmetrical topology and small-scale energy requirements. The introduction of technical specifications of the aesthetic and ergonomic type relates the product to the user, allowing it to operate in an intuitive and simple way although the product incorporates a highly complex technology. The current trend in design is to create products which are integrated into the environment. Thus incorporating an aesthetic value in the rotors helps to improve the natural and architectural environment, while humanizing a complex technology [45]. EcoDesign is a growing trend that integrates multifaceted aspects of design and environmental considerations. The objective is to create sustainable solutions that satisfy human needs and desires [46]. Following these lines of work some researchers have designed vertical rotors capable of incorporating aesthetic-ergonomic criteria used in the design of products for the design of the geometry of their buckets, maintaining their technical performance. The vertical rotor described in the patent [47] uses the value of the golden Ratio as the dimensioning parameter of its buckets. The topology of the buckets in the rotor is given by a convex surface generated from logarithmic spirals obtained from the value of the golden ratio. In this regard, the patent [48] describes a vertical rotor whose buckets consist of a spiral-shaped frame whose dimensions are also based on the values of the golden ratio. Unfortunately both rotors do not meet the requirement of lateral accessibility to their inside zone, and are therefore difficult to apply to consumer products.

Introducing aesthetic criteria in vertical rotors at the commercial level is a growing trend nowadays. The Hercules rotor of the Enessere company [49] introduces harmonic requirements into its design, offering great advantages in its setting inside any landscape context, even one of high aesthetic prestige. This rotor has recently been awarded the 2016 Silver Design Award [50]. For the particular use of Savonius rotors adapted to consumer products, the newly constructed artificial tree L'arbre du Vent [51] operates as a small local power generating network in which each bucket (Aeroleaf) is a small wind turbine. The Aeroleaf is able to take advantage of the slightest wind breeze regardless of the direction of origin, this being optimal for the use of the product in an urban environment. The organic and biomimetic modeling [52] of the surface of the buckets makes them integrate into the environment, differentiating them from the conventional ones. The Wind Tulip turbines from the Leviathan Energy Company [53] are vertical rotors of the Savonius type, which combine aerodynamics and industrial design in the same way, requiring low wind speed to generate energy, being quiet and requiring low maintenance.

The paper presents the numerical-experimental study carried out on a new rotor adapted from a canonical Savonius rotor to which a set of geometric and topological requirements have been introduced. These new requirements cause changes in its geometry which allow the new rotor to be part of sustainable consumer products. The performance of the turbine has been analyzed for different rotation angles of its buckets by means of testing different wind speeds within a range of tip speed ratios. The new power coefficient, torque coefficient, and generated power have been calculated. The new rotor incorporates a parametrized design with geometric variables based on aesthetic specifications. The geometric operations applied to the canonical Savonius rotor have changed the curvature of its buckets by means of transforming the initial cylindrical surfaces into surfaces of an organic type that can be perfectly integrated into the architectural or particular environments which usually present these kinds of shapes. The new rotor features have all the advantages of the Savonius rotor such as self-starting, ease of manufacture and maintenance and operation at low wind speeds, as well as accessibility to its inside zone. The parameterization of variables allows obtaining rotors of different sizes which, when incorporated into sustainable products meet their design requirements while satisfying their functional requirements. While the new rotor partly sacrifices its performance it nevertheless meets the aesthetic and ergonomic requirements of the product, making it easier to sell while still meeting its energy requirements. The new rotor is born as a suitable variant of the Savonius rotor for small scale energy applications and for its application in products where aesthetic requirements need to be combined with a functional performance.

2. Description of the new rotor geometry

In order to validate the influence of the aesthetic and ergonomic requirements on the performance of the $\mathcal{S}$ Savonius vertical rotor, three prototype rotors $\mathcal{P}_j$ have been designed and manufactured based on the $\mathcal{S}$ geometry. The new buckets of the rotors $\mathcal{P}_j$ have been obtained by means of geometric operations based on symmetry of translation, rotation and scale on the cross sections [r_{s1i}, r_{s2i}] of the canonical $\mathcal{S}$ rotor. With this procedure it is possible to obtain a set of new profiles [$r_{\mathcal{P}j1i}$, $r_{\mathcal{P}j2i}$] for the buckets of $\mathcal{P}_j$ on which a subsequent sweep operation is achieved. The curvature of the buckets of the canonical $\mathcal{S}$ rotor is transformed from cylindrical surfaces to organic ruled surfaces.

The geometry of the Savonius $\mathcal{S}$ rotor (Fig 1) is encompassed within the scope of the symmetrical bodies. The symmetrical shapes present a set of potentially beneficial qualities for the designers since they allow the creation of harmonious, interesting and memorable designs. Symmetry is associated with beauty and is a geometric property found in almost all forms of nature. This is the reason why they tend to draw attention in the environment in which they are located. There are three types of basic symmetry; reflection symmetry, translational symmetry and rotation symmetry [54]. The three prototype rotors $\mathcal{P}_j$ have been designed to fulfill these three types of symmetry.

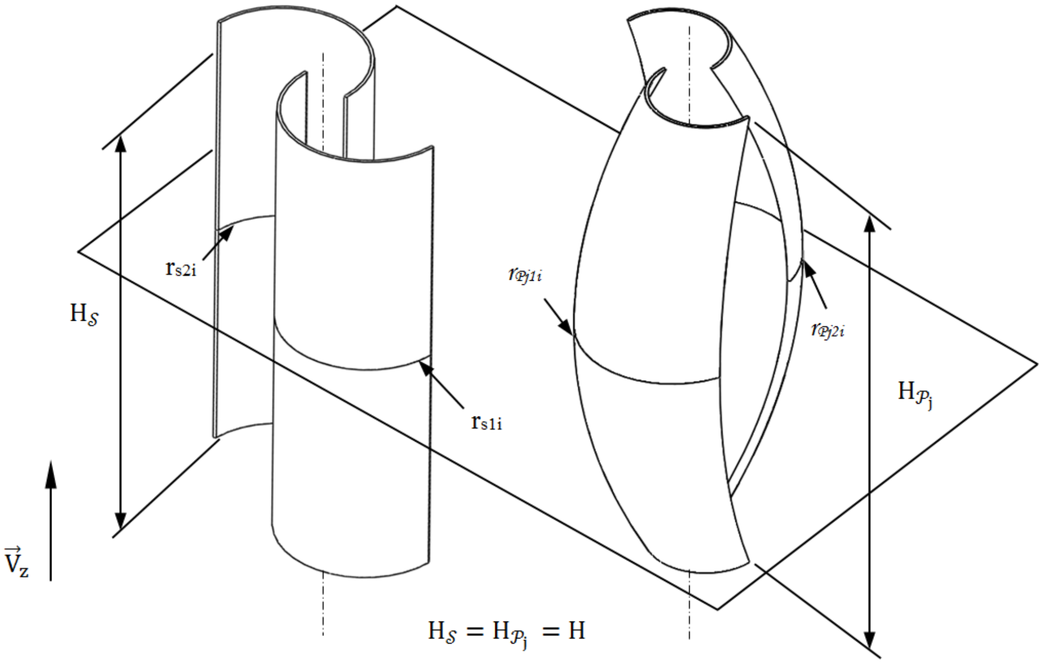

Fig 1.- Representation of a generic Π_i cutting plane and the sections [r_{s1i}, r_{s2i}] ∈ $\mathcal{S}$ *and* [$r_{\mathcal{P}j1i}$, $r_{\mathcal{P}j2i}$] ∈ $\mathcal{P}_j$.

2.1.- Application of the translational symmetry operation to the sections coincident with the mean plane of the rotor Savonius

The sections [r_{s1i}, r_{s2i}] ∈ $\mathcal{S}$ coinciding with the mean plane of the rotor ($i = \frac{H}{2}$) are separated from each other by a distance e_x along the X axis equal to the distance necessary to be able to locate an element $\mathcal{A}$ with radio a_{shaft} (Fig 2) in the inside zone of the buckets $\mathcal{B}_{\mathcal{S}}$.

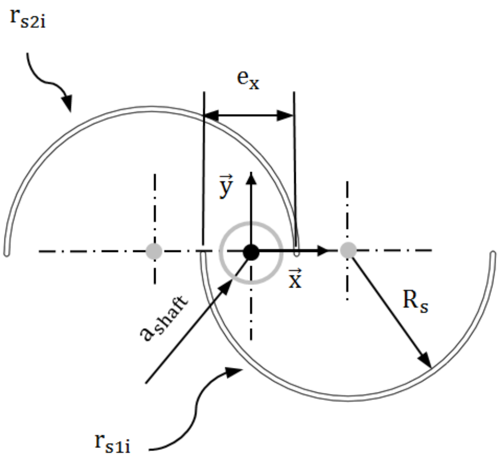

Fig 2.- Application of the translation symmetry operation to the sections [r_{s1i}, r_{s2i}] ∈ $\mathcal{S}$ coincident with the mean plane of the rotor ($i = \frac{H}{2}$).

In order to fulfill the ergonomic requirement of lateral accessibility to the inside element $\mathcal{A}$, the sections [r_{s1i}, r_{s2i}] ∈ $\mathcal{B}_{\mathcal{S}}$ are again displaced on the plane $\Pi_{\frac{H}{2}}$ by a length L_a along the direction $\overrightarrow{L_a}$ Eq. (1)-(2). As shown in Fig 3. $C_{\mathcal{S}}$ represents the center of [r_{s1i}, r_{s2i}] ∈ $\mathcal{B}_{\mathcal{S}}$, u_x [m] represents the displacement of [r_{s1i}, r_{s2i}] along the X axis, and u_y [m] the displacement of the sections along the Y axis. In this way it has been possible to locate two new sections [$r_{\mathcal{P}j1i}$, $r_{\mathcal{P}j2i}$] for $i = \frac{H}{2}$ which act as base profiles of the new prototype rotor geometry $\mathcal{P}_j$ according to the geometric requirement of translation symmetry. The distance L_a Eq. (2) between each pair of sections [$r_{\mathcal{P}j1i}$, $r_{\mathcal{P}j2i}$] of the buckets

$\mathcal{B}_{\mathcal{P}\mathrm{j}}$ is parameterized so that different sized rotors can be obtained by simply replacing the design variables established in the paper. Eq. (3)-(5).

$$\overrightarrow{\mathrm{L_a}} = u_x \,.\, \vec{x} + u_y \,.\, \vec{y} \quad (1)$$

$$L_a = \left|\overrightarrow{\mathrm{L_a}}\right| = \sqrt{u_{x+}^2\, u_y^2} \quad (2)$$

$$\mathrm{e_{p_x}} = \mathrm{e_x} + 2 \cdot |\mathrm{u_x}| \quad (3)$$

$$\mathrm{e_{p_y}} = \mathrm{e_y} + 2 \cdot |\mathrm{u_y}| = 2 \cdot |\mathrm{u_y}\,| \quad (4)$$

$$\mathrm{e_y} = 0 \quad (5)$$

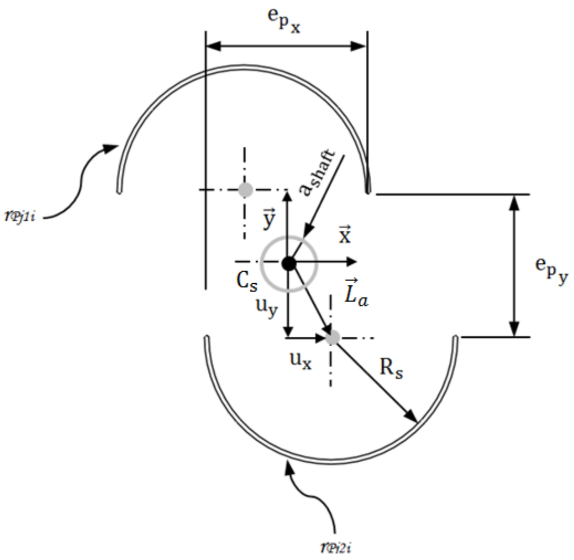

Fig 3.- Obtaining the profiles $[r_{\mathcal{P}j1i}, r_{\mathcal{P}j2i}] \in \mathcal{B}_{\mathcal{P}j}$ *for a height* $i = \frac{H}{2}$.

As shown in Fig 3, the geometric definition of each section $[\mathrm{r_{s1i}}, \mathrm{r_{s2i}}] \in \mathcal{B}_{\mathcal{S}}$ and $[r_{\mathcal{P}j1i}, \mathrm{r}_{\mathcal{P}j2i}] \in \mathcal{B}_{\mathcal{P}\mathrm{j}}$ that lies at a height $\mathrm{i} = \frac{\mathrm{H}}{2}$ can be expressed in parametric form as indicated in Table 1, Eqs(6)-(9).

Savonius rotor	$\mathrm{r_{s_{1i}}} = [\mathrm{R_s} - \frac{\mathrm{e_x}}{2} \quad 0] + \mathrm{R_s} \cdot \big(\mathrm{Cos}(\vartheta), \mathrm{Sin}(\vartheta)\big)\ \forall\ \vartheta \in [0, \pi)$ (6)
	$\mathrm{r_{s_{2i}}} = [-\mathrm{R_s} + \frac{\mathrm{e_x}}{2} \quad 0] + \mathrm{R_s} \cdot \big(\mathrm{Cos}(\vartheta), \mathrm{Sin}(\vartheta)\big)\ \forall\ \vartheta \in [0, \pi)$ (7)
Prototype rotors	$\mathrm{r_{p_{j1i}}} = [-\mathrm{R_s} + \frac{\mathrm{e_{p_x}}}{2} \quad \frac{\mathrm{e_{p_y}}}{2}] + \mathrm{R_s} \cdot \big(\mathrm{Cos}(\vartheta), \mathrm{Sin}(\vartheta)\big)\ \forall\ \vartheta \in [0, \pi)$ (8)
	$\mathrm{r_{p_{j2i}}} = [\mathrm{R_s} - \frac{\mathrm{e_{p_x}}}{2} \quad -\frac{\mathrm{e_{p_y}}}{2}] + \mathrm{R_s} \cdot \big(\mathrm{Cos}(\vartheta), \mathrm{Sin}(\vartheta)\big)\ \forall\ \vartheta \in [\pi, 2\pi)$ (9)

Table 1.- Parametric equations of the sections $[r_{s1i}, r_{s2i}] \in \boldsymbol{\mathcal{B}_{\mathcal{S}}}$ *and* $[r_{Pj1i}, r_{Pj2i}] \in \boldsymbol{\mathcal{B}_{\mathcal{P}j}}$ *for* $i = \frac{\boldsymbol{H}}{\boldsymbol{2}}$.

The radius $\mathrm{R_P}$ of the buckets $\mathcal{B}_{\mathcal{P}\mathrm{j}}$ for the sections $[r_{\mathcal{P}1i}, r_{\mathcal{P}2i}]$ at a height $\mathrm{i} = \frac{\mathrm{H}}{2}$ is analogous to the radius $\mathrm{R}_{\mathcal{S}}$ of the sections $[\mathrm{r_{s1i}}, \mathrm{r_{s2i}}]$ of the canonical Savonius rotor with buckets $\mathcal{B}_{\mathcal{S}}$.

2.2.- Application of the geometric scaling operation between the sections of the ends of the rotor Savonius. Obtaining sections belonging to the new rotor

In order to obtain the final geometry of the prototype rotors $\mathcal{P}_j$, the sections $[r_{s1i}, r_{s2i}]$ of the ends of the rotor $\mathcal{S}$ are displaced by a distance L_a along the X and Y axis, subsequently applying a reducing scale factor equal to the golden number ϕ. In this way, the geometric features of the new sections $[r_{\mathcal{P}j1i}, r_{\mathcal{P}j2i}]$ Eqs. (10)-(11) for i = 1, H can be related through the criterion of golden proportionality with the sections $[r_{\mathcal{P}j1i}, r_{\mathcal{P}j2i}]$ for i= $\frac{H}{2}$. Finally the set of sections $[r_{\mathcal{P}j1i}, r_{\mathcal{P}j2i}]$ for heights i= 1, $\frac{H}{2}$, H are joined by means of two 3D spline topology guide curves linking three points P_i contained in each section $[r_{\mathcal{P}j1i}, r_{\mathcal{P}j2i}]$ Fig 4. The spline curves are used as a spine for the sweep operation of the set of sections $[r_{\mathcal{P}j1i}, r_{\mathcal{P}j2i}]$,obtaining the final surface of the new buckets $\mathcal{B}_{\mathcal{P}j}$. Table 2 shows the parametric equations for the sections $[r_{\mathcal{P}j1i}, r_{\mathcal{P}j2i}]$ for height i = 1, H.

Prototype rotors	$r_{p_{j1i}} = \frac{1}{\phi} \cdot r_{p_1} = \frac{1}{\phi} \cdot \left(\left[-R_s + \frac{e_{p_x}}{2} \quad \frac{e_{p_y}}{2} \right] + R_s \cdot (\mathrm{Cos}(\vartheta), \mathrm{Sin}(\vartheta)) \; \forall \; \vartheta \in [0, \pi) \right)$ (10)
	$r_{p_{j2i}} = \frac{1}{\phi} \cdot r_{p_2} = \frac{1}{\phi} \cdot \left(\left[R_s - \frac{e_{p_x}}{2} \quad -\frac{e_{p_y}}{2} \right] + R_s \cdot (\mathrm{Cos}(\vartheta), \mathrm{Sin}(\vartheta)) \; \forall \; \vartheta \in [\pi, 2\pi) \right)$ (11)

Table 2.- Parametric equations of the sections $[r_{Pj1i}, r_{Pj2i}] \in \mathcal{P}_j$ for height values i = 1, H.

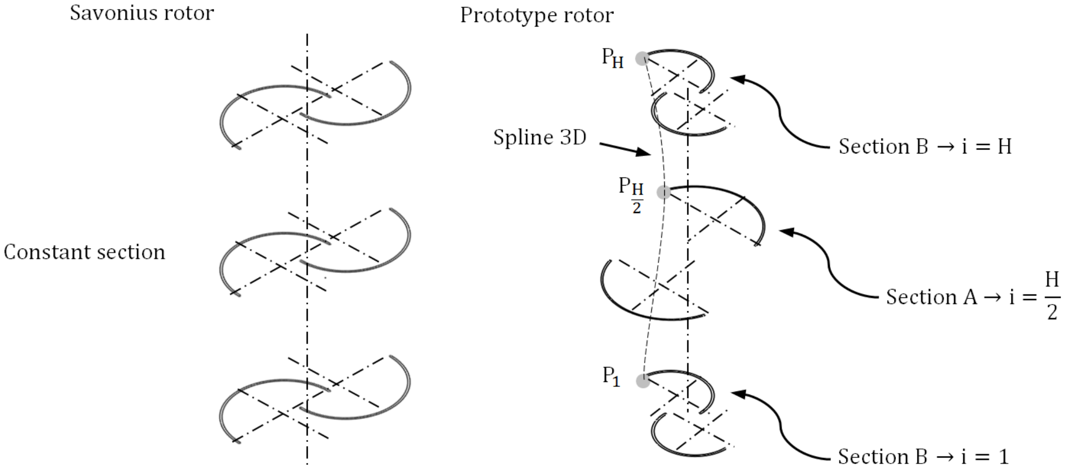

Fig 4.- Obtaining of the guide curves in the geometric operation of sweep along the sections in the rotors $\mathcal{P}_j$.

2.3.- Application of the rotation symmetry operation to the sections del nuevo rotor $\mathcal{P}$. Rotation angle δ for heights coinciding with the middle and extreme planes

Another topological feature of the Savonius rotors is the geometrical transformation of their buckets by applying rotational operations, thus obtaining helical Savonius rotors. This is in order to fulfill the aesthetic requirement of rotation symmetry between its buckets $\mathcal{B}_{\mathcal{P}j}$. This operation has been applied to the sections $[r_{\mathcal{P}j1i}, r_{\mathcal{P}j2i}]$ for values i= 1, $\frac{H}{2}$, H, δ equal to 0^o, 22^o y 45^o respectively, obtaining three prototype rotors $\mathcal{P}_j$ that meet the design requirement.

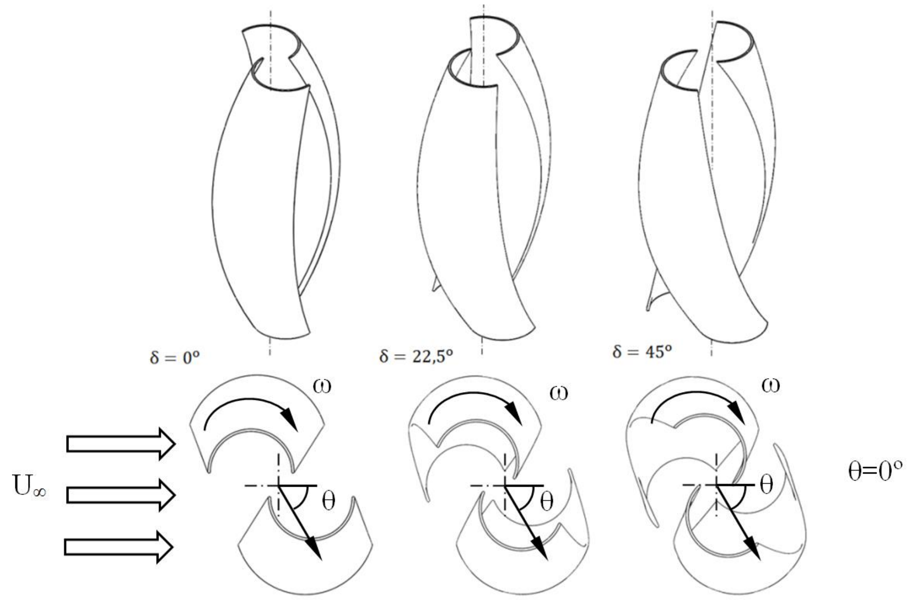

Fig. 5.- Obtaining the three prototype rotors $\mathcal{P}_j$ for values of δ equal to 0º, 22º y 45º.

The new $\mathcal{P}$ rotor has been designed in a parametric way which allows the obtaining of the prototype $\mathcal{P}_j$ rotors by only modifying the value of the parameter δ. In order to validate the performance of the new rotor the values of the design variables have been established according to the dimensions of one of the products that the $\mathcal{P}$ rotor will be part of [55], one application is [56]. For this product dimensions related to lateral accessibility and ergonomics have been obtained from the standard anthropometric measurements of the hand of an adult man [57]. In Table 3 the magnitude of the set of geometric features is shown for both the canonical Savonius rotor $\mathcal{S}$ and the set of prototype $\mathcal{P}_j$ rotors analyzed in the present paper (see Fig 5).

Savonius rotor $\mathcal{S}$	
R_s [mm]	57,5
e_x [mm]	37,5
e_y [mm]	0
a_{shaft} [mm]	14,5
H_s [mm]	320,0

Prototype rotors $\mathcal{P}_j$ for i= $\frac{H}{2}$	
R_s [mm]	57,5
e_{p_x} [mm]	68,5
e_{p_y} [mm]	99,4
u_x [mm]	15,5
u_y [mm]	49,7
a_{shaft} [mm]	14,5
H_p [mm]	320,0

Table 3.- Dimensions of the canonical Savonius rotor $\boldsymbol{\mathcal{S}}$ and the prototype $\boldsymbol{\mathcal{P}_j}$ rotors.

3. Experimental set-up and methodology

In order to analyze the mechanical behavior of each designed rotor, they were tested by means of a low-speed jet-type wind tunnel (see Fig.6), whose testing trasversal area is 400 mm x 400 mm with a total length of the test channel of 1500 mm. The uniform main flow in the tunnel is produced by a 5 kW rotating fan with a variable speed drive engine, so the flow can reach a maximum speed of 40 m/s. The wind speed has been adjusted for each geometry analyzed according to the given Reynolds number and the maximum allowable speed that the rotors can withstand without load conditions. As is shown in Fig 6 the wind tunnel was provided with a honeycombe-shaped plates system. Thus, the wind tunnel gave a turbulence level of less than 2%, and a high ratio of flow uniformity. The wind speed is determined by a pitot tube connected to a manometer (Testo 512).

Fig 6.- Wind tunnel of the Higher Polytechnic School of the University of Jaen, fluid mechanics research group.

The maximum size of the bounding box of each rotor tested in this study was 200 mm x 200 mm x 320 mm. As shown in Fig 8, the prototype rotors were located at a distance of 900 mm downstream from the entrance of the rectangular test channel. The rotors were fixed to a base composed of two circular plates in the center of which a bearing is located to allow rotation of the axis of the rotors minimizing the friction (see Fig 7). This base was manufactured in PLA, using the additive manufacturing technique by means of flux deposition. The rotors were fixed to the shaft by means of threaded lugs housed in the rotor supports. The base was attached to the lower surface of the wind tunnel by means of a set of washers and screws. In addition, the center of rotation of the prototype rotors was aligned with the mass center of the main wind area of the tunnel channel, to avoid any kind of eccentricity. The application of this test methodology facilitates the replacement of the rotors for the different analyses performed.

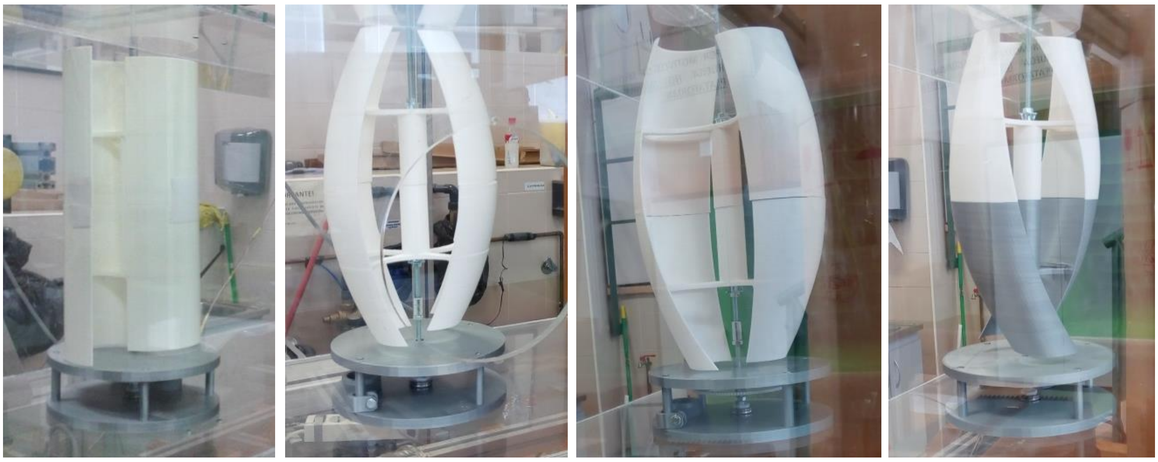

Fig. 7.- Rotors $\mathcal{S}$ and $\mathcal{P}_j$ fixed to the wind tunnel by means of a circular PLA base.

The rotors were placed inside the wind tunnel through a circular window of 200 mm, located at the top of the tunnel. As can be seen in Fig. 6, the length of the rotor shaft is greater than the section height of the tunnel. This allows a direct torque measurement on the rotor shaft with a "Prony brake system" dynamometer and a speed measurement of the rotor through a conventional tachometer, both installed outside the wind tunnel over the ceiling of the testing space. Fig. 8 shows the layout of the arrangement of the main elements and tools used in the rotor tests.

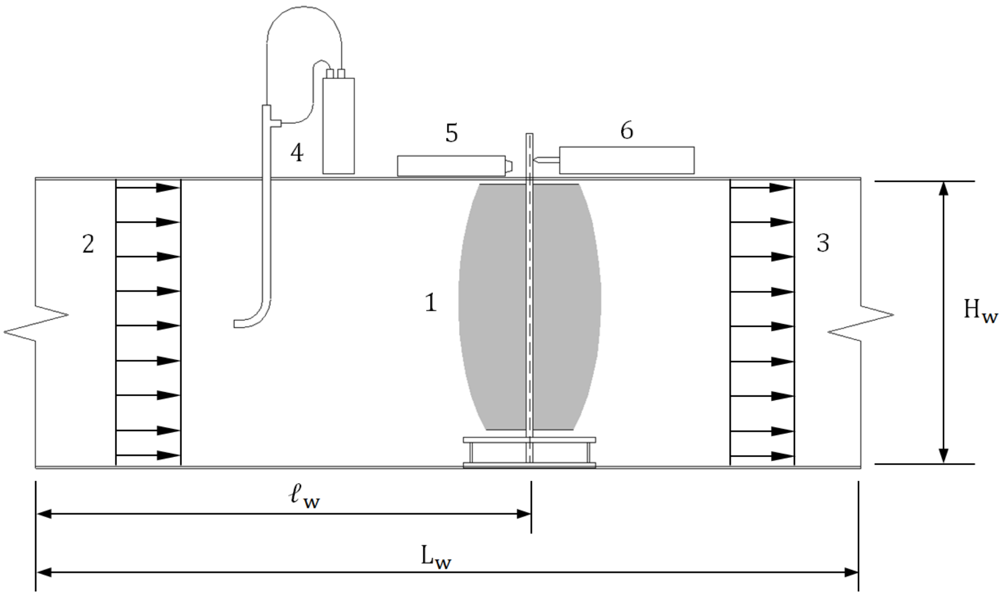

Fig 8.- Schematic diagram of the set-up.

1	Vertical rotor turbine	4	Pitot tuve and manometer
2	Upstream air flow	5	Photo tachometer
3	Downstream air flow	6	Dynamomter

Table 4.- Components of the schematic set-up diagram.

To build the “Prony brake system” a PCE-FB50 dynamometer was used positioned at 30 mm from the turbine axis pointing to a torque arm which is jointed to the rotor shaft with an adjustable brake. The PCE-FB50 dynamometer has a measurement range of between 0 and 50 N, 0.01 N of resolution and an accuracy of ±0.01 N. To determine the power developed by the turbine it is also necessary to measure turbine speed, therefore a Digital Photo Tachometer model RM-1501 was used as well. The experimental devices were used to predict the static torque of the rotor at a given rotational speed and investigate the conditions experienced by the proposed wind turbines placed in the uniform air flow.

In addition, it is important to note that the results obtained cannot be acquired or compared with results obtained in a non-uniform fully external flow. Therefore, the jet-type wind tunnel (see Fig 6) has been an important tool for obtaining a non-turbulent uniform flow to characterize the power and moment coefficient curves versus tip speed ratio of the prototype rotors $\mathcal{P}_j$.

4. Data Reduction

The expression of the Reynolds number Eq. (12) used in the present paper uses as characteristic length the diameter of the prototype rotors and as characteristic speed the speed of the wind tunnel uniform air flow.

$$\mathrm{Re} = \frac{\rho \cdot \mathrm{U}_\infty \cdot \mathrm{D}}{\mu} \quad (12)$$

Where Re is the Reynolds number, U_∞ [m/s] is the wind tunnel uniform air flow velocity, D is the prototype rotor, ρ [kg/m^3] is the density of air and μ [Pa·s] is the absolute viscosity of air.

The expression of the dimensionless speed number, tip speed ratio Eq. (13), is given by.

$$\mathrm{TSR} = \frac{\omega \cdot \mathrm{D}}{2 \cdot \mathrm{U}_\infty} \quad (13)$$

Where ω [rad/s] is the angular velocity of the prototype rotors.

The magnitude of the force obtained by the dynamometer allows us to determine the moment Eq. (14) that the prototype rotor exerts on its axis of rotation by means of the following expression.

$$\mathrm{T_s} = \mathrm{F_{din}} \cdot \mathrm{l}\ (14)$$

Where $\mathrm{T_s}$ [N·m] is the static torque derived from the prototype rotors, $\mathrm{F_{din}}$ [N] is the magnitude of the force obtained by the dynamometer and l [m] the radial distance between the point of measurement or location of the dynamometer and the center of rotation of the prototype rotor.

Statics torque coefficient ($\mathrm{C_{ts}}$), torque coefficient ($\mathrm{C_t}$) and power coefficient ($\mathrm{C_p}$) Eqs. (15)-(17) were given as follows:

$$\mathrm{C_{ts}} = \frac{4 \cdot \mathrm{T_s}}{\rho \cdot \mathrm{U}_\infty^2 \cdot \mathrm{D}^2 \cdot \mathrm{H}}\ (15)$$

$$\mathrm{C_t} = \frac{4 \cdot \mathrm{T}}{\rho \cdot \mathrm{U}_\infty^2 \cdot \mathrm{D}^2 \cdot \mathrm{H}}\ (16)$$

$$\mathrm{C_p} = \mathrm{C_{ts}} \cdot \mathrm{TSR} = \frac{4 \cdot \mathrm{T_s} \cdot \omega \cdot D}{\rho \cdot \mathrm{U}_\infty^2 \cdot \mathrm{D}^2 \cdot \mathrm{H} \cdot 2 \cdot \mathrm{U}_\infty} = \frac{2 \cdot \mathrm{T_s} \cdot \omega}{\rho \cdot \mathrm{U}_\infty^3 \cdot \mathrm{D} \cdot \mathrm{H}}\ (17)$$

Where T [N·m] is the dynamic toque derived from the prototype rotors.

The aspect ratio ($\mathrm{A_R}$) Eq. (18) represents the height of the prototype rotors relative to their diameter. The prototype rotors proposed in this paper are governed by the golden ratio, so the value of this dimensionless parameter is equal to the golden number (ϕ).

$$\mathrm{A_R} = \frac{\mathrm{H}}{\mathrm{D}} \approx \phi\ (18)$$

Where H [mm] is the height and D [m] is the diameter of the prototype rotors.

The overlap ratio (β_x, β_y) Eq. (19) is a dimensionless parameter relative to the separation distance between the buckets of the prototype rotors $\mathcal{B}_{\mathcal{P}j}$ versus their diameter (see Fig 3). The expression of this dimensionless parameter is given as follows.

$$\beta_x = \frac{\mathrm{e}_{\mathrm{p}_x} - \mathrm{a_{shaft}}}{2 \cdot \mathrm{R_s}} \quad ; \quad \beta_y = \frac{\mathrm{e}_{\mathrm{p}_y} - \mathrm{a_{shaft}}}{2 \cdot \mathrm{R_s}}\ (19)$$

Where $\mathrm{e}_{\mathrm{p}_x}$ [m] is the separation distance between the buckets of the prototype rotors on the coordinate axis X, $\mathrm{e}_{\mathrm{p}_y}$[m] is the separation distance between the buckets of the prototype rotors on the coordinate axis Y, d [m] is the characteristic measure of the prototype buckets and $\mathrm{a_{shaft}}$ [m] is the diameter of object $\mathcal{A}$, housed inside the rotor (aligned with the axis of the object).

Table 5 shows the magnitude of the dimensionless geometric parameters for both the canonical Savonius rotor model and the set of prototype rotors.

	$\mathrm{A_R}$	β_x	β_y
Savonius rotor	1.618	0.343	0.000
Prototype rotors	1.618	0.326	0.611

Table 5.- Dimensionless geometric parameters of the prototype rotors and the canonical Savonius rotor.

Finally, the blockage ratio (B) Eq. (20) represents the area of the prototype rotors bounding box relative to the cross area of the wind tunnel.

$$\mathrm{B} = \frac{\mathrm{H} \cdot \mathrm{D}}{\mathrm{H_{wt}} \cdot \mathrm{W_{wt}}}\ (20)$$

Where $\mathrm{H_{wt}}$ [m] is the cross area height of the wind tunnel and $\mathrm{W_{wt}}$ is the cross area width of the wind tunnel. Considering Fig 8, the magnitudes of the geometric parameters of the section of the wind tunnel are the same because it has a square shape. Therefore, substituting the overlap ratio in the expression of the blockage ratio (B) Eq. (21).

$$B = \frac{H \cdot D}{2D \cdot 2D} = \frac{H}{4 \cdot D} = \frac{\phi}{4} \approx 0.405 \quad (21)$$

The maximum blockage ratio is within 40.5% for all the prototype rotor models studied in this paper.

5. Numerical method

In order to compare and discuss the experimental results of the present study, a numerical analysis was carried out using a Computational Fluid Dynamics (CFD) commercial software of the different geometries studied for different load scenarios. The commercial software used to perform numerical analysis is Ansys Fluent [58]. Fluent is a Computational Fluid Dynamics software which by means of the mathematical and numerical technique of the finite volumes solves problems of fluid mechanics and transfer of heat around or within geometries with complex surfaces. The modeling of the simulation is performed considering three-dimensional effects given that the geometry of the prototype rotors is not constant along the axial direction, as shown in the CAD modeling Fig 5. Modeling of the CAD geometry of the rotors and the solid volume of the wind tunnel was performed by using Solidworks [59]. A guided process that offers the interface of the numerical calculation program allows the usual tasks of the process to be performed. These tasks consist of the selection of the physical model of calculation used, the selection and physical characteristics of the fluid and solid materials of the problem, all cell zone conditions, boundary conditions, solution methods and the turbulence model. After that, the values of limit conditions, maximum number of iterations and convergence criteria are defined in order to achieve the numerical analysis.

5.1. Computation domains and boundary conditions

The definition of the computational domain of the different numerical analyses was carried out considering the dimensions of the wind tunnel used. As shown in Fig 9, the dimensions of the computational domain are 2D x 2D x 6.5D, where D [m] is the diameter of the helices. In addition, from the surfaces of this domain, the boundary conditions corresponding to the stationary and moving walls, the uniform inlet airflow and the outlet airflow were defined.

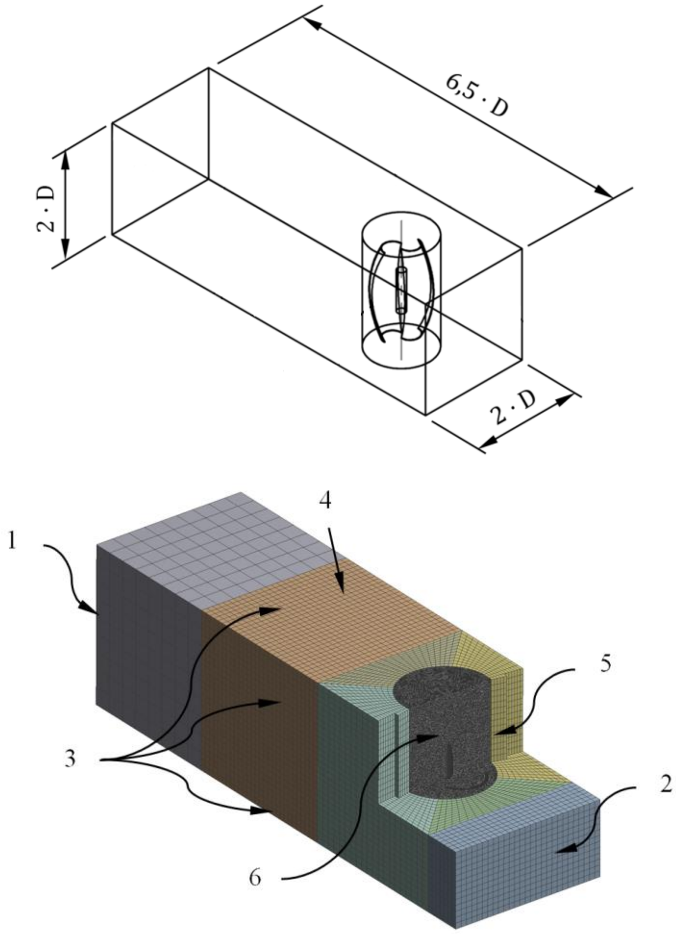

Fig 9.- Representation of the computational domain used in the numerical analysis.

1	Pressure outlet	4	Wind tunnel domain
2	Velocity inlet	5	Interface rotor-tunnel domain
3	Static walls, No-Slip Walls	6	Rotor domain

Table 6.- Boundary conditions and computing domain.

The boundary condition of shear type in the walls of the rotors and in the side walls of the wind tunnel domain has been defined as ‘No-Slip Walls’. The definition of this boundary condition contributes to the formation of a boundary layer near the walls of the rotors. The problem presented in this paper does not imply the use of a deformable mesh. Therefore a sliding mesh model was applied to perform the rotational motion of the rotor and analyze its dynamic behavior. Inside the wind tunnel domain a cylindrical domain, where the geometries of the rotors are included, is generated. This domain, called Rotor domain, is independent of the wind tunnel domain. This second domain is located at a distance downstream of 1.5D from the inlet uniform airflow surface and centered on the Wind tunnel domain.

This methodology is simpler and more efficient in comparison with the dynamic mesh model analysis. The technique consists of the realization of a steady model in which the definition of the cell zone condition for the Rotor domain is a moving reference frame, determining the speed (obtained through the experimental tests) and axis of rotation of the prototype rotors. After that, a transient model is generated in which the definition of the cell zone condition for the Rotor domain is obtained by copying the results of the Reference frame model to the section Mesh Motion. One interface surface is performed at the overlap edges between the adjacent domains, the rotor-tunnel domain, allowing the continuity of the solution in the air flow.

A uniform and steady velocity profile is applied at the boundary condition of the velocity inlet. Specification method parameters used in the turbulence definition for the velocity inlet and pressure outlet are intensity and length scale, see Table 7. The walls of the Wind tunnel domain are defined as stationary static walls and the walls of the prototype rotors, with their respective axes and speeds of rotation, are defined as moving walls.

Intensity	5 %
Length scale	0.1 [m]

Table 7.- Intensity and turbulence length.

For all numerical analyses performed, the input parameters were supported by experimental data. Therefore, the rotational velocities of the prototype rotors studied for the Rotor domain were defined according to the rotational velocities measured during the experimental test in the wind tunnel. Best parameters were acquired comparing performance values acquired by different prototype rotor geometries.

5.2. Mesh definition

In order to compare experimental and numerical results and to improve numerical precision, mesh modeling was performed adaptively for each computational domain. The perturbations in the fluids are of the same magnitude order as the objects which cause it, and for this reason aerodynamic studies often use mesh models between 10 and 20 times larger than the size of the airfoils, as Bangga observes [66]; although in the present paper the lateral walls of the tunnel used for the experimental tasks have been included in the mesh, precisely because their proximity can have an effect on the behavior of the turbine. For this reason the sliding mesh is defined within a perimeter of 40 cm x 40 cm in order to compare the numerical study with the experimental test. On the other hand it has been considered that the zones linked through non-conformal interfaces of the sliding meshes remain in contact with each other, and in that way the air will be able to flow from one domain to the other. The mesh node density used in the rotor domain is higher than in the wind tunnel domain, as is shown in Fig 10. In addition, the geometry of the elements forming the meshes varies for each computational domain. In the case of the Rotor domain, tetrahedral elements with smaller size are used, which allows us to adapt with greater pressure to the geometry of prototype rotor geometries. On the contrary, for the Wind tunnel domain hexahedral elements are used since the size of this domain is greater and these elements improve the time and computational cost of the studies. The selection of tetrahedral elements for the Rotor domain penalizes the computational cost of the simulations; however, it improves the accuracy and adaptability of the mesh to the prototype rotor geometries.

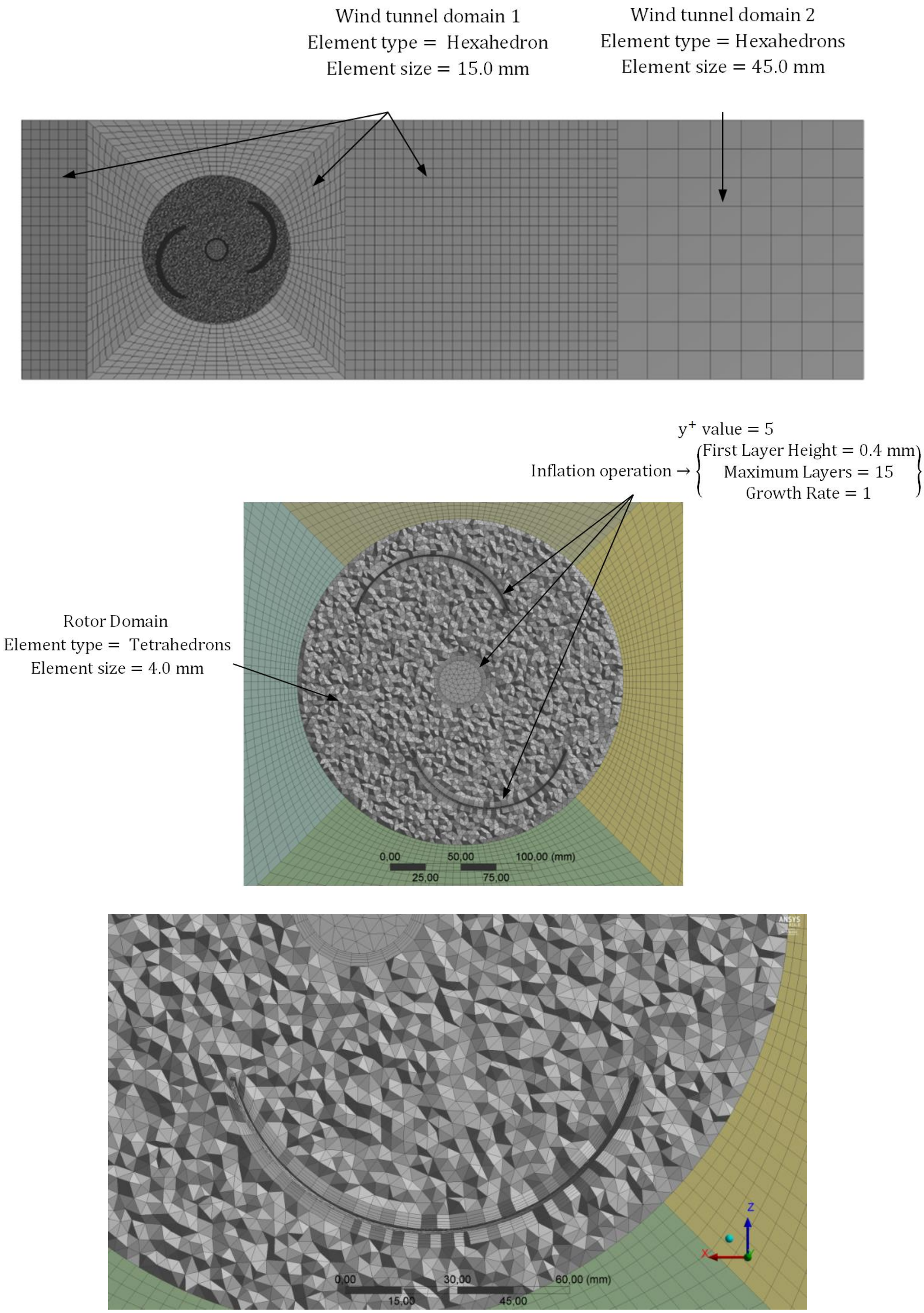

Fig 10.- Grid generation for the static domain and the boundary layers.

Table 8a shows the grid points on the Rotor domain along streamwise and spanwise directions.

	Streamwise	Spanwise
Savonius rotor $\mathcal{S}$	64	118
Prototype rotor $\mathcal{P}_j$ for value of δ equal to 0º	61	113
Prototype rotor $\mathcal{P}_j$ for value of δ equal to 22,5º	60	114
Prototype rotor $\mathcal{P}_j$ for value of δ equal to 45º.	62	115

Table 8a.-Number of grid points on the Rotor domain along streamwise and spanwise directions.

Table 8b shows the grid points along the streamwise and spanwise directions and along the contour of the buckets of the rotors. This grid points number corresponds to the 'inflation' meshing operation performed in order to improve the numerical analysis solution in the geometry regions near the wall of the buckets (the shear layer).

	Streamwise	Spanwise	Buckets contour
Savonius rotor $\mathcal{S}$	5	81	100
Prototype rotor $\mathcal{P}_j$ for value of δ equal to 0º	5	92	79
Prototype rotor $\mathcal{P}_j$ for value of δ equal to 22,5º	5	92	79
Prototype rotor $\mathcal{P}_j$ for value of δ equal to 45º.	5	92	79

Table 8b.-Number of grid points on the buckets along its contour and streamwise and spanwise directions.

The elements of the mesh are three-dimensional because the geometry of the prototype rotors varies along their rotation axis (axial coordinate). In Table 9, the values of the characteristics parameters used in the modeling of the different meshes are shown.

	Savonius rotor	Prototype rotors		
		$\delta = 0^o$	$\delta = 22.5^o$	$\delta = 45^o$
Average ortogonal quality	0.8138	0.8169	0.8170	0.8174
Input tetrahedral element size [mm]	4.0	4.0	4.0	4.0
Input hexahedral element size [mm]	15.0/45.0	15.0/45.0	15.0/45.0	15.0/45.0
Number of elements	2316895	2319440	2323401	2323825
Number of nodes	3527442	3492860	3506757	3504981

Table 9.- Characteristic parameters of the meshes generated for each study geometry.

Where orthogonal quality represents the quality of the elements of the mesh through a range from 0 to 1, with 0 being the low quality indicative.

Finally, in order to enhance the accuracy of the numerical analysis in the boundary layer flow and improve the mesh quality, prismatic mesh elements were extruded from the boundary edges of the prototype buckets. (See Fig. 10). The modeling of these elements of the mesh was carried out by means of an inflation operation. The parameters used for the definition of this operation are shown in Fig 10. These establish a y^+ value of the first elements from the wall equal to 5, given the rotational velocity and the position of the elements on the buckets (see Fig 10). This value y^+ is constant for all the geometries analyzed and allows a precise analysis of the boundary layer in the walls of the buckets [61]. In addition, for the numerical analyses carried out, a wall function of the 'Enhanced wall treatment' type was used. This wall treatment combines a two-layer model with enhanced wall functions. It should be noted that the modeling of the surface roughness is not compatible with the wall function established for the turbulence model used. Furthermore, in order to avoid problems of continuity between the different computational domains, a contact surface is established that allows interaction between them.

5.3. Turbulence model, governing equations and simulation set up

The viscosity model used in this study is Realizable $k - \varepsilon$ with a logarithmic surface function in the analysis of turbulence flow. The Realizable k-ε model includes the effects of mean rotation in the definition of the turbulent viscosity inside the equations, in order to avoid the insensitivity to adverse pressure gradients of the standard k-ε model. This extra rotation effect has been tested on single sliding mesh systems and shown superior behavior over the standard k-ε model [65], or even the SST k-ω model in those cases where the turbulence was established, because the k-ω method has been calibrated to accurately compute flow separation. Nevertheless, due to the nature of the mean rotation modification, its application to multiple sliding meshes systems should be taken with some caution, because several rotating meshes can avoid the rotation turbulent effect added to the equations in some of the meshes. In the present paper, several turbulence models have been used, and finally with the realizable k-ε model the numerical results are closer to the experimental data [63]. Other authors studying VAWT type Savonius use the RNG k-ε model [62] or directly the Standard k-ε model [64], mainly because these turbines work with the drag force effect, instead of lift force as occurs with other airfoil applications.

Momentum equations, x, y, z velocity components, turbulent kinetic energy (k) and the specific dissipation rate of turbulent kinetic energy (ε) Eqs. (22)-(28) are the variables that were resolved by using CFD Fluent software [58]. The equations of mass protection, momentum protection, stress tensor, turbulence viscosity, turbulence kinetic energy and dissipation rate of turbulence kinetic energy can be expressed for the compressible and incompressible steady flows as follows in the Cartesian tensor rotation [60]:

- Continuity equation:

$$\frac{\partial}{\partial x_w} \cdot (\rho \cdot u_w) = 0 \ (22)$$

- Momentum equation:

$$\frac{\partial}{\partial x_w} \cdot (\rho \cdot u_w \cdot u_v - \tau_{vw}) = \frac{\partial P}{\partial x_w} \ (23)$$

Where x_j represents the cartesian coordinate, being $j = 1, 2, 3$, u_j represents the absolute velocity components in the x_w direction. $P_l = {}^{\partial P}/_{\partial x_w}$ represents the reduced pressure loss and τ_{vw} represents the stress tensor as follows:

- Stress tensor equation:

$$\tau_{vw} = \mu \cdot \left(\frac{\partial u_v}{\partial x_w} + \frac{\partial u_w}{\partial x_v} - \frac{2}{3} \cdot \frac{\partial u_k}{\partial x_k} \cdot \delta_{vw}\right) \ (24)$$

$$\forall \{v, w\} \mid v \neq w \rightarrow \delta_{vw} = 0 \ (25)$$

$$\forall \{v, w\} \mid v = w \rightarrow \delta_{vw} = 1 \ (26)$$

Where μ is the viscosity of the air and δ_{vw} is the Kronecker delta variable. The Kronecker delta variable takes a zero value when the values v and w are different. On the other hand, when the variables v and w are equal the Kronecker delta variable takes value 1.

- Turbulence kinetic energy (k):

$$\frac{\partial}{\partial t}(\rho \cdot k) + \frac{\partial}{\partial x_w} \cdot \left(\rho \cdot u_w \cdot k - \frac{\mu_{eff}}{\sigma_k} \cdot \frac{\partial k}{\partial x_w}\right) = \mu_t \cdot s_{vw} \cdot \frac{\partial u_v}{\partial x_w} - \frac{2}{3} \cdot \left(\mu_t \cdot \frac{\partial u_v}{\partial x_w} + \rho \cdot k\right) \cdot \frac{\partial u_v}{\partial x_w} - \rho \cdot \varepsilon \ (27)$$

- Dissipation rate of turbulence kinetic energy (ω)

$$\begin{aligned} &\frac{\partial}{\partial t}(\rho \cdot \omega) + \frac{\partial}{\partial x_w} \cdot \left(\rho \cdot u_w \cdot \omega - \frac{\mu_{eff}}{\sigma_\varepsilon} \cdot \frac{\partial \varepsilon}{\partial x_w}\right) \\ &= C_1 \cdot f_1 \cdot \frac{\varepsilon}{k} \cdot \left[\mu_t \cdot s_{vw} \cdot \frac{\partial u_v}{\partial x_w} - \frac{2}{3} \cdot \left(\mu_t \cdot \frac{\partial u_v}{\partial x_w} + \rho \cdot k\right) \cdot \frac{\partial u_v}{\partial x_w} \cdot \delta_{vw}\right] - c_2 \cdot f_2 \cdot \rho \cdot \frac{\varepsilon^2}{k} - C_3 \cdot \rho \cdot \varepsilon \cdot \frac{\partial u_v}{\partial x_w} \ (28) \end{aligned}$$

Where the effective viscosity Eq. (29) is.

$$\mu_{eff} = \mu + \mu_t \ (29)$$

Being.

$$\mu_t = \rho \cdot f_\mu \cdot C_\mu \cdot \frac{k^2}{\varepsilon} \ (30)$$

Table 10, shows the values defined in the numerical calculation software for the variables $v, w, k, C_\mu, \sigma_k, \sigma_\varepsilon, C_{1\varepsilon}, C_{2\varepsilon}$ of the equations shown above [60].

v, w, k	1, 2, 3
C_μ	0.09
σ_k	1.00
σ_ε	1.30
$C_{1\varepsilon}$	1.44
$C_{2\varepsilon}$	1.92

Table 10.- Values of the main parameters of the governing equations.

This turbulence model does not require the implementation of transition models since it is valid only for flows developed in complete turbulence [65]. All the above equations were resolved by means of an iterative numerical calculation process, in which the Coupled analysis algorithm is used in order to calculate the field of velocities and pressures in the central point of each mesh elements.In addition, the terms of the second order of pressure, moment, turbulent kinetic energy (k), the specific dissipation rate of turbulent kinetic energy (ω), given in the equations governing the numerical model, are included in the calculation in order to match the numerical result with the experimental results. Furthermore, pressure correction is resolved in order to maintain the availability of the pressure area and mass protection in each iteration.

The number of Courant, CFL used in each numerical analysis is 200. Finally, Table 11 shows the Time step size, Number of time steps and Max iterations used for each numerical analysis. The time step was defined from the rotational speed of the rotors obtained in the experimental tests. For the numerical analysis of the rotors, an experimental value of the wind tunnel velocity and a rotary speed value of the rotors were used, respectively (each rotor has a characteristic speed for a given mechanical load and wind speed). From this rotation speed, the Time step corresponding to the 30º rotation in each rotor was obtained for the different numerical analyses carried out.

	Time Step Size (s)	Number of Time Steps	Max Iterations
Savonius rotor $\mathcal{S}$	0,0049	18	20
Prototype rotor $\mathcal{P}_j$ for value of δ equal to 0º	0,0129180	18	500
	0,0070319	18	500
Prototype rotor $\mathcal{P}_j$ for value of δ equal to 22,5º	0,012256	18	1000
	0,005140	18	500
Prototype rotor $\mathcal{P}_j$ for value of δ equal to 45º.	0,0101014	18	1000
	0,0057100	18	500

Table 11.-Time step size, Number of time steps and Max iterations employed for each rotor in the numerical analyses.

6. Results and discussion

The set of prototype rotors $\mathcal{P}_j$ presented in this paper together with the Savonius $\mathcal{S}$ canonical rotor were tested in the range of wind speeds between 2.56 m/s and 10.6 m/s. According to the methodology used to perform the experimental tests, each rotor was tested for the different positions of the Prony brake. And for each of these positions of the Prony brake, Reynolds numbers between 3,436 · 104 and 1,419 · 105 were tested to characterize the behavior of the rotors in all their operating regimes. The objectives of the experimental tests were the determination of the parameters power coefficient, torque coefficient and mechanical power generated. In turn, in order to perform a validation of the methodology used a set of numerical analyses were modeled using the Ansys Fluent software [58], whose results allowed us to determine the evolution of the parameters under study along the circular path of the rotors and contrast those results with those obtained experimentally. The experimental data of the force variables applied by the rotor F_{din} [N] and the rotational speed of the rotors ω [rad/s] were acquired according to the precision and resolution of the measurement instruments used, the PCE-FB50 dynamometer and Digital Photo Tachometer model RM-1501, respectively.

The graphs of power coefficient, torque coefficient and power of the prototype rotors were compared to each other for different magnitudes of the rotation angle parameter, $\delta = 0^o, 22.5^o, 45^o$. This parameter represents the rotation or torsion angle between the main sections of the prototype rotors (see Fig 5). The torque coefficient profiles versus the rotational angle of the prototype rotors were compared with the profile obtained by the canonical Savonius rotor, for a wind speed of 5.331 [m /s] and Reynolds number $7.137 \cdot 10^4$ (See Fig 14). In addition, the maxima in the power coefficient curves versus tip speed ratio of the prototype rotors were evaluated and compared with the values obtained in the power coefficient curve of the canonical Savonius rotor for the same magnitude of tip speed ratio of the maximums obtained (see Table 12). In this way, the influence of the geometric modifications performed in the prototype rotors with respect to the Savonius canonical rotor geometry can be determined for the study parameters: power coefficient, torque coefficient and mechanical power generated.

6.1. *Effect of rotation or torsion angle δ*

Figs 11, 12 and 13 show the power coefficient and torque coefficient versus tip speed ratio; the mechanical power generated versus the angular velocity of rotation; and the wind tunnel velocity versus the rotors angular velocity for the prototype rotors with different rotation or torsion angles ($\delta = 0^{o}, 22.5^{o}, 45^{o}$) and for the canonical Savonius rotor. It may be observed that as the rotation angle δ increases, the maximum value of the curves of both power coefficient and mechanical power generated increase. Similarly, the tip speed ratio associated with these maxima (see Table 12) increases. This fact indicates that as the rotation angle δ increases, the angular velocity of the prototype rotors increases and thus the power coefficient curve is shifted towards values of tip speed ratio and higher power coefficient, improving the performance and behavior of the prototype rotors.

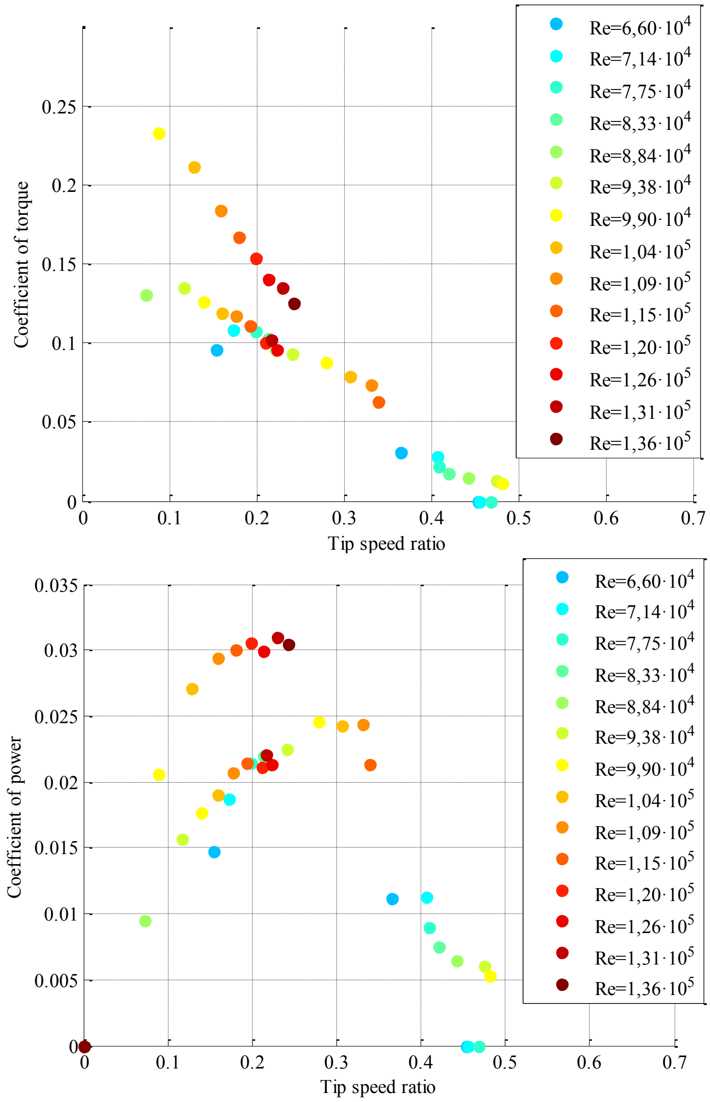

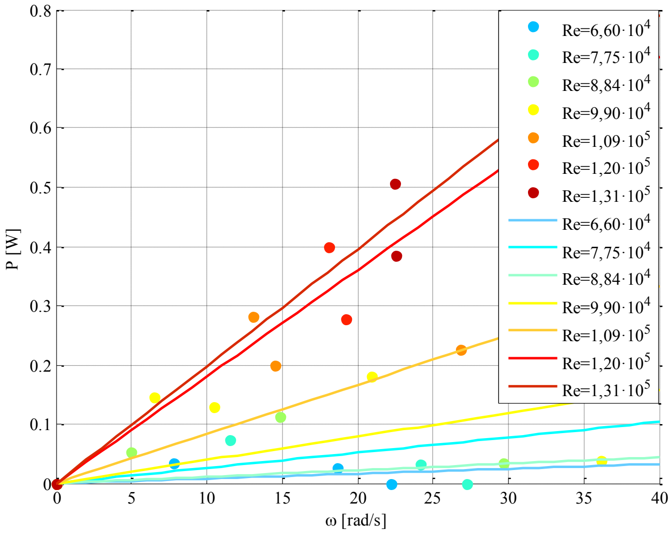

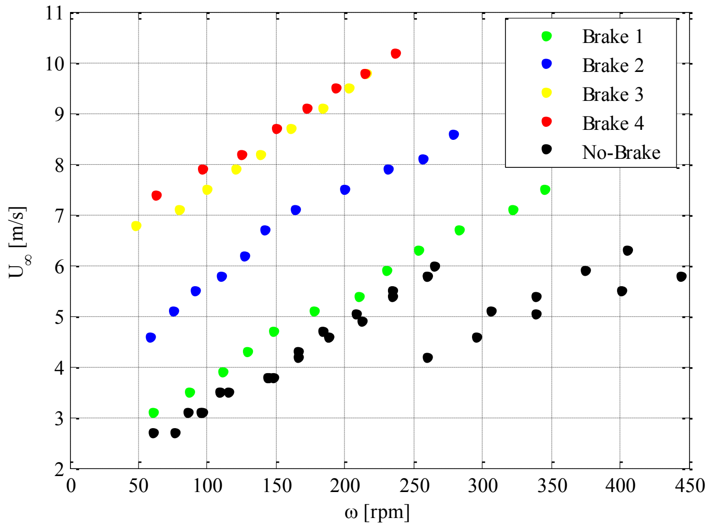

Fig 11.- Curves of power coefficient, Torque coefficient, Mechanical power and Wind tunnel velocity vs Angular rotor velocity for the prototype rotor δ=0º.

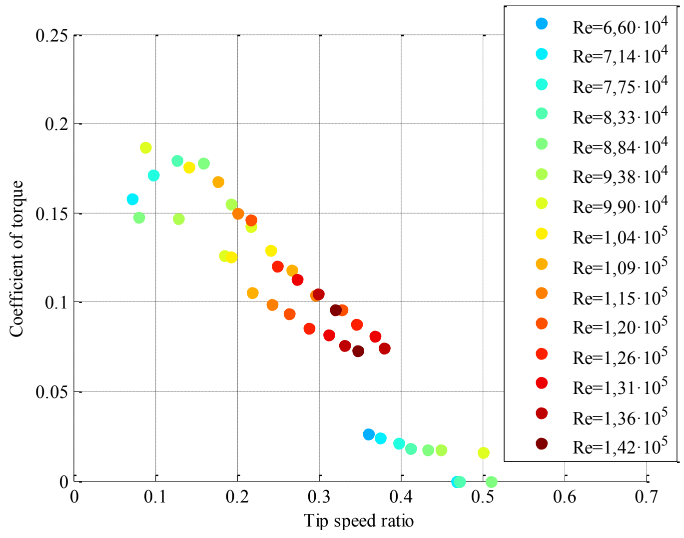

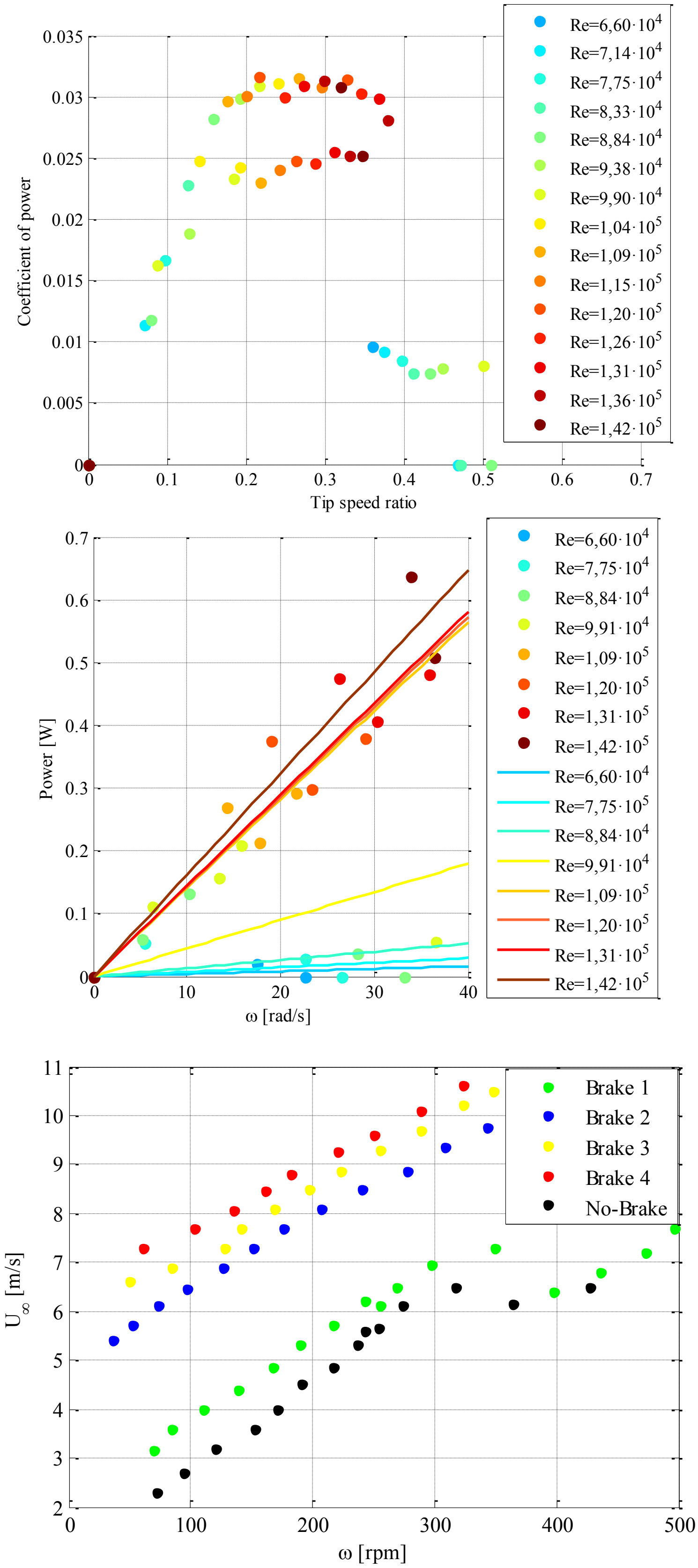

Fig. 12.- Curves of power coefficient, Torque coefficient, Mechanical power and Wind tunnel velocity vs Angular rotor velocity for the prototype rotor δ=22.5º.

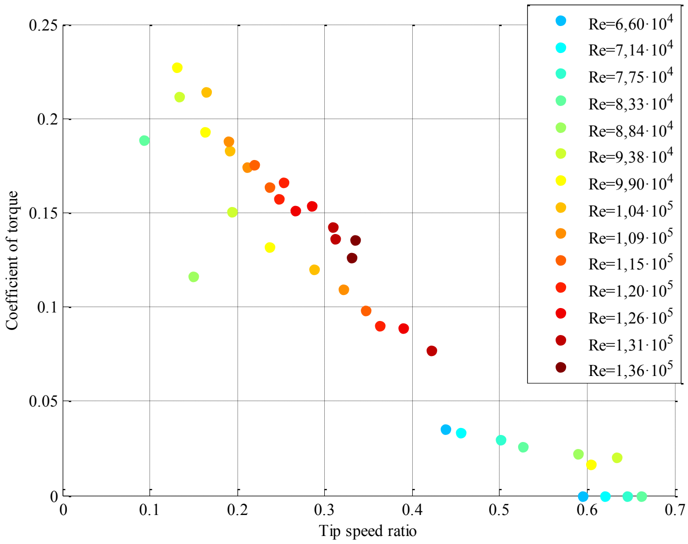
Coefficient of torque
Tip speed ratio
0
0.05
0.1
0.15
0.2
0.25
0
0.1
0.2
0.3
0.4
0.5
0.6
0.7
$Re=6,60\cdot 10^{4}$
$Re=7,14\cdot 10^{4}$
$Re=7,75\cdot 10^{4}$
$Re=8,33\cdot 10^{4}$
$Re=8,84\cdot 10^{4}$
$Re=9,38\cdot 10^{4}$
$Re=9,90\cdot 10^{4}$
$Re=1,04\cdot 10^{5}$
$Re=1,09\cdot 10^{5}$
$Re=1,15\cdot 10^{5}$
$Re=1,20\cdot 10^{5}$
$Re=1,26\cdot 10^{5}$
$Re=1,31\cdot 10^{5}$
$Re=1,36\cdot 10^{5}$

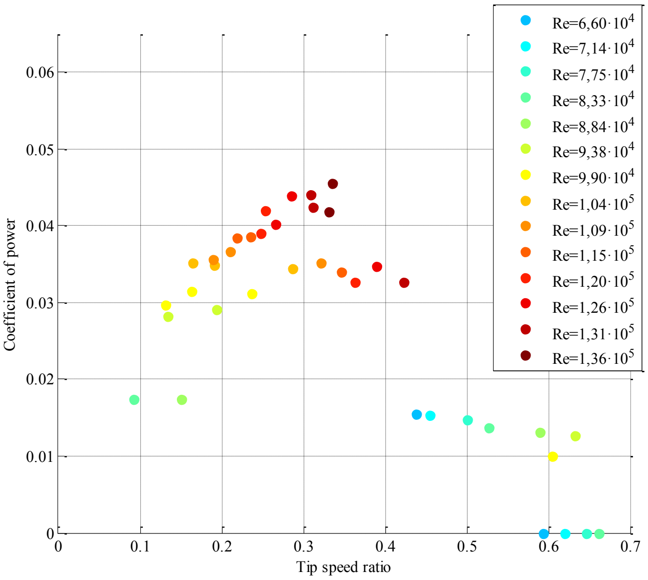
Coefficient of power
Tip speed ratio
0
0.01
0.02
0.03
0.04
0.05
0.06
0
0.1
0.2
0.3
0.4
0.5
0.6
0.7
$Re=6,60\cdot 10^{4}$
$Re=7,14\cdot 10^{4}$
$Re=7,75\cdot 10^{4}$
$Re=8,33\cdot 10^{4}$
$Re=8,84\cdot 10^{4}$
$Re=9,38\cdot 10^{4}$
$Re=9,90\cdot 10^{4}$
$Re=1,04\cdot 10^{5}$
$Re=1,09\cdot 10^{5}$
$Re=1,15\cdot 10^{5}$
$Re=1,20\cdot 10^{5}$
$Re=1,26\cdot 10^{5}$
$Re=1,31\cdot 10^{5}$
$Re=1,36\cdot 10^{5}$

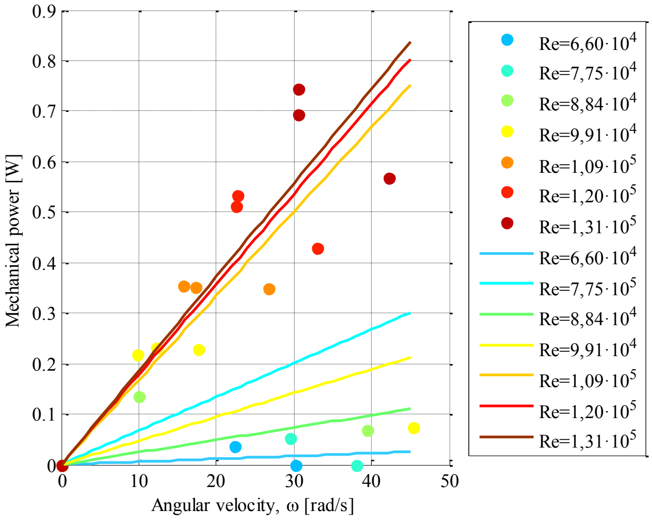
Mechanical power [W]
Angular velocity, ω [rad/s]
0
0.1
0.2
0.3
0.4
0.5
0.6
0.7
0.8
0.9
0
10
20
30
40
50
$Re=6,60\cdot 10^{4}$
$Re=7,75\cdot 10^{4}$
$Re=8,84\cdot 10^{4}$
$Re=9,91\cdot 10^{4}$
$Re=1,09\cdot 10^{5}$
$Re=1,20\cdot 10^{5}$
$Re=1,31\cdot 10^{5}$
$Re=6,60\cdot 10^{4}$
$Re=7,75\cdot 10^{5}$
$Re=8,84\cdot 10^{4}$
$Re=9,91\cdot 10^{4}$
$Re=1,09\cdot 10^{5}$
$Re=1,20\cdot 10^{5}$
$Re=1,31\cdot 10^{5}$

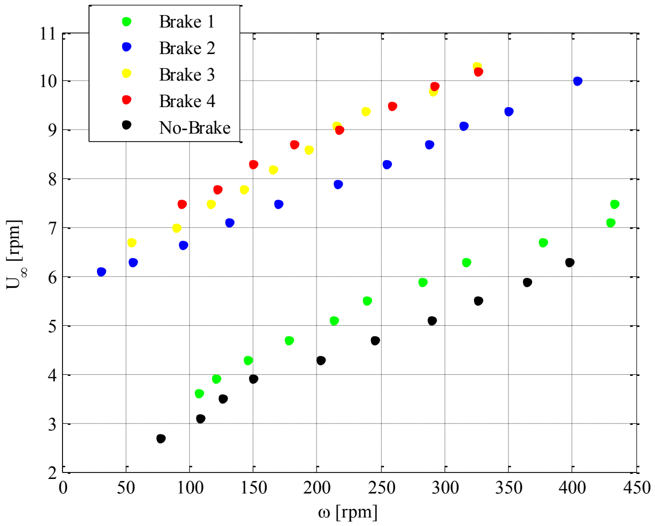

Fig. 13.- Curves of power coefficient, Torque coefficient, Mechanical power and Wind tunnel velocity vs Angular rotor velocity for the prototype rotor δ=45º.

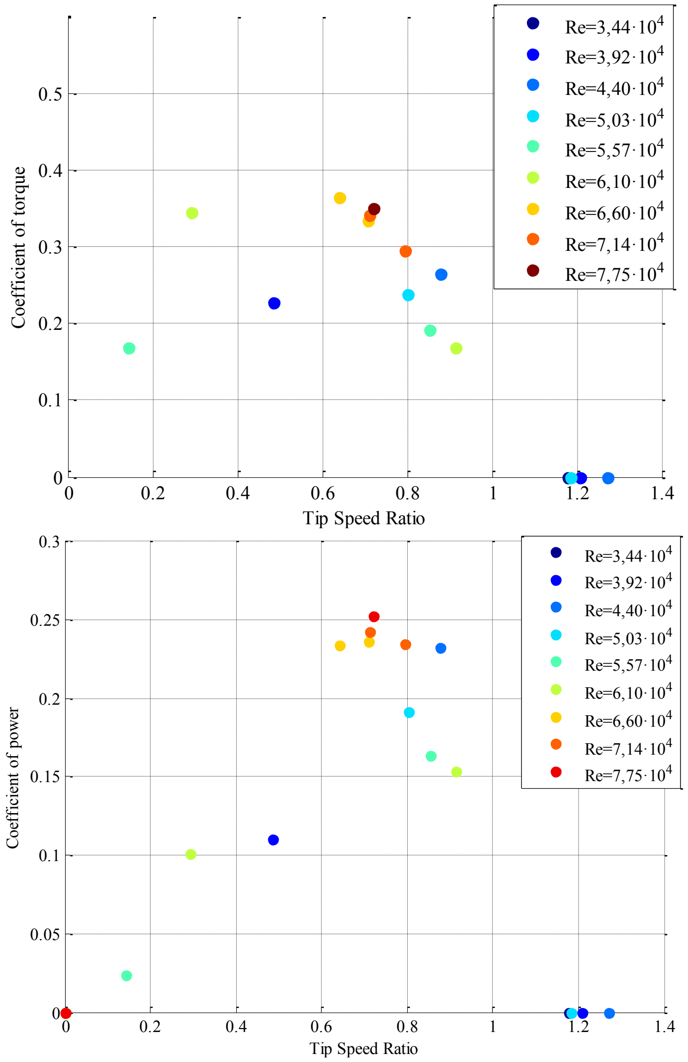

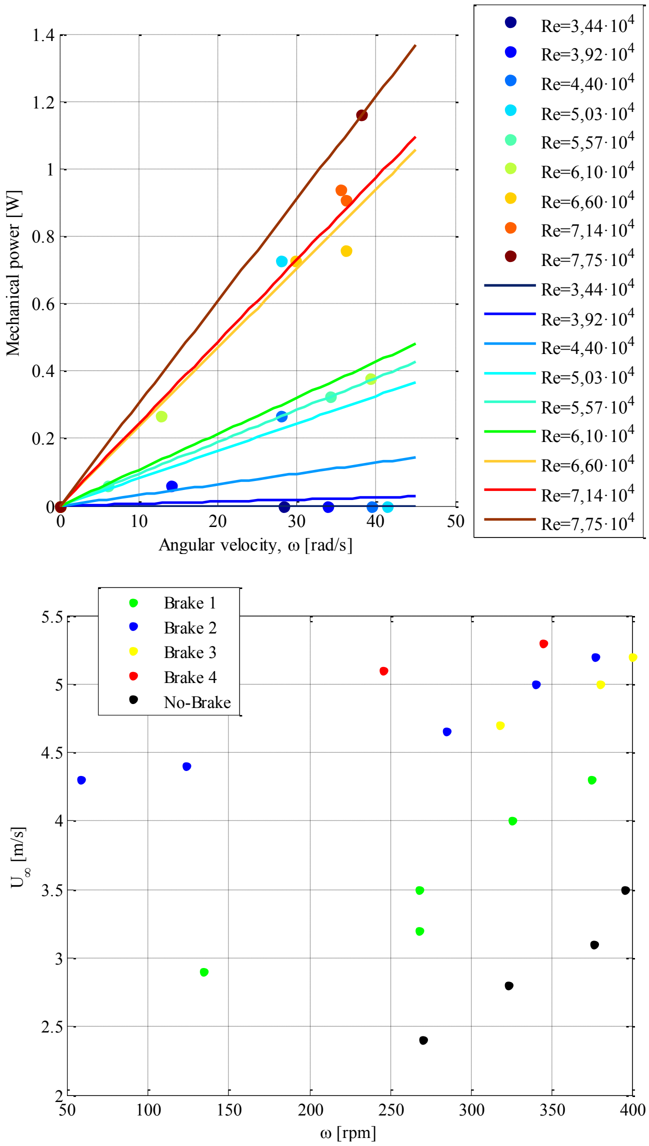

Fig 14.- Curves of power coefficient, Torque coefficient, Mechanical power and Wind tunnel velocity vs Angular rotor velocity for the canonical Savonius rotor.

Prototype rotors	$C_{p_{max}}$	Corresponding Re at $C_{p_{max}}$	TSR at $C_{p_{max}}$	$C_{t_{max}}$	Corresponding Re at $C_{t_{max}}$	TSR at $C_{t_{max}}$	P_{max}	Corresponding Re at P_{max}	ω at P_{max} [rad/s]
δ = 0°	0.031	$1.36 \cdot 10^5$	0.229	0.233	$9.91 \cdot 10^4$	0.089	0.562	$1.36 \cdot 10^5$	24.81
δ = 22.5°	0.032	$1.20 \cdot 10^5$	0.217	0.186	$9.91 \cdot 10^4$	0.087	0.637	$1.42 \cdot 10^5$	33.92
δ = 45°	0.046	$1.36 \cdot 10^5$	0.335	0.227	$9.91 \cdot 10^4$	0.131	0.744	$1.31 \cdot 10^5$	30.61
Savonius rotor	0.252	$7.75 \cdot 10^4$	0.721	0.364	$6.60 \cdot 10^4$	0.642	1.611	$7.75 \cdot 10^4$	38.22

Table 12.- Maximum values of the curves Ct vs TSR, Cp vs TSR and P vs ω.

Table 12, shows the maximum values of the power coefficient, torque coefficient and mechanical power generated parameters, as well as the tip speed ratio and the Reynolds number from which these maximum values are calculated. Table 12 shows the difference in the tip speed ratio range for optimal rotor performance between the canonical Savonius $\mathcal{S}$ rotor and the prototype rotors. While in the prototype rotors the tip speed ratio range for optimum operation is 0.229, 0.217 and 0.335 for Reynolds numbers of $1.364 \cdot 10^5$, $1.203 \cdot 10^5$, $1.364 \cdot 10^5$, in the Savonius $\mathcal{S}$ canonical rotor the tip speed ratio for optimum rotor performance is 0.721 for a Reynolds number of 77482.923. That is to say, the tip speed ratio of the optimal operating range of the prototype rotors is lower than that of the Savonius $\mathcal{S}$ canonical rotor, and on the contrary the Reynolds number for the optimal operating range of the prototype rotors is higher than that of the rotor Savonius $\mathcal{S}$ canonical. Therefore, it can be observed that in order to reach the optimum operating range for prototype rotors the wind speed must be higher compared to the Savonius $\mathcal{S}$ canonical rotor, since these tend to rotate at a lower angular velocity than the canonical Savonius one. This fact can be checked by evaluating the mechanical power generated, because for the prototype rotors the maximum mechanical power generated (0.562 W, 0.637 W, 0.744 W, respectively) reaches a higher number of Reynolds ($1.364\cdot10^5$, $1.203\cdot10^5$, $1.364\cdot10^5$, respectively) and a lower angular speed of rotation (24.81 rad/s, 33.92 rad/s, 30.61 rad/s, respectively) compared to the canonical Savonius rotor (mechanical power generated 1.611 W, Reynolds number 77482.923, angular speed of rotation 38.22 rad /s).

6.2. Effect of the coefficient of power, coefficient of torque and Reynolds number

Table 13, shows the different Reynolds numbers and their corresponding wind speeds from which the prototype rotors and the Savonius canonical rotor were tested. Figs 11,12,13 and 14 show the variation of the power coefficient for prototype rotors with a rotation or torsion angle in the bucket section of $\delta = 0^\circ, 22.5^\circ, 45^\circ$ and for the canonical Savonius rotor. According to these results, it is observed that the maximum coefficient of power increases with the increase of the Reynolds number. This fact is also reported by Kamoji et al. [11] and Akwa et al. [21] for conventional Savonius rotors. Furthermore, it is the tip speed ratio at which the maximum coefficient of power, $C_{p_{max}}$ increases with the increase of the Reynolds number from $6.599\cdot10^4$ to $.419\cdot10^5$ (prototype rotor) and $3.436\cdot10^4$ to $6.097\cdot10^4$ (Savonius rotor).

Figs 11, 12, 13 and 14 show the torque coefficient variation for prototype rotors with a rotation or torsion angle in the bucket section of $\delta = 0^\circ, 22.5^\circ, 45^\circ$ for the canonical Savonius rotor. The results obtained show that the Reynolds number influences the profiles of the torque coefficient curves. The torque coefficient decreases linearly as the tip speed ratio values increase. However, the trend of the torque coefficient as a function of the Reynolds number is not linear. The torque coefficient increases until the Reynolds number reaches its maximum $C_{t_{max}}$ at a Reynolds number of $9.907\cdot10^4$ for the three prototype rotors $\mathcal{P}_j$ and $6.599\cdot10^4$ for the Savonius $\mathcal{S}$ (See table 13). From this value, the maximum torque coefficient for each Reynolds number decreases as the Reynolds number increases.

Prototype rotors	
Reynolds number	Wind velocity[m/s]
$6.599\cdot10^4$	4.929
$7.137\cdot10^4$	5.331
$7.748\cdot10^4$	5.787
$8.327\cdot10^4$	6.220
$8.848\cdot10^4$	6.609
$9.378\cdot10^4$	7.005
$9.907\cdot10^4$	7.400
$1.044\cdot10^5$	7.800
$1.094\cdot10^5$	8.172
$1.152\cdot10^5$	8.606
$1.203\cdot10^5$	8.988
$1.258\cdot10^5$	9.400
$1.311\cdot10^5$	9.794
$1.364\cdot10^5$	10.190
$1.419\cdot10^5$	10.600

Savonius rotor	
Reynolds number	Wind velocity[m/s]
$3.436\cdot10^4$	2.567
$3.916\cdot10^4$	2.925
$4.398\cdot10^4$	3.285
$5.026\cdot10^4$	3.754
$5.574\cdot10^4$	4.164
$6.097\cdot10^4$	4.554

Table 13.- Reynolds number and wind velocity at which the prototype rotors and the canonical Savonius rotor were tested.

6.3. Correlations for performance of prototype rotors and comparison with the numerical analysis

As shown in Figs. 15 and 16, as the Reynolds number increases the power coefficient and torque coefficient curves have variations. In the case of the power coefficient curves, as the Reynolds number increases the magnitude of the power coefficient increases similarly until the maximum power coefficient $C_{p_{max}}$ (see table 12) is reached in the parabolic profile. On the other hand, in the case of the torque coefficient curves, as the Reynolds number increases the torque coefficient increases until it reaches its maximum value $C_{t_{max}}$ (see table 12). From this maximum value, the torque coefficient begins to decrease as the Reynolds number increases. This whole set of curves (torque coefficient versus tip speed ratio curve and power coefficient versus tip speed ratio curve) can be unified in a single curve that approximates the fluid-mechanical behavior of the rotors independently to the evolution of the Reynolds number, as shown in Figs. 15 and 16.

The correlation equation used is a second-order polynomial function $\frac{\mathrm{C_t}}{\mathrm{Re^n}}$ Eq. (31). To obtain the coefficients that define the correlation equation, the torque coefficients of each prototype rotor were divided by the Reynolds number corresponding to each point, raised to a dimensionless factor n (see Fig 15 and 16). The curve $\frac{\mathrm{C_t}}{\mathrm{Re^n}}$ versus the tip speed ratio is interpolated from a second-order polynomial in order to obtain the coefficients that define the correlation equation (see table 14). It should be noted that for prototype rotors with a rotation angle δ equal to 0^{o} and 45^{o} the correlation equation was applied to points in the torque coefficient curve with a Reynolds number greater than $9.907 \cdot 10^4$, while for the prototype rotor with a rotational angle δ equal to 22.5^{o} the correlation equation was applied for points in the torque coefficient curve with a Reynolds number greater than $7.137 \cdot 10^4$. In this way, lower Reynolds numbers are depreciated where the viscous stresses and the peeling of the boundary layer can cause a distortion in obtaining the correlation equation.

$$\frac{\mathrm{C_t}}{\mathrm{Re^n}} = \mathrm{p_3} \cdot \mathrm{TSR}^2 + \mathrm{p_2} \cdot \mathrm{TSR} + \mathrm{p_1} \ (31)$$

		n	Correlation equation	R – Square
Prototype rotors	$\delta = 0^{\mathrm{o}}$	0.3	$\frac{\mathrm{C_t}}{\mathrm{Re^{0.3}}} = -0.025855 \cdot \mathrm{TSR} + 0.0097774$	99.50 %
	$\delta = 22.5^{\mathrm{o}}$	1.5	$\frac{\mathrm{C_t}}{\mathrm{Re^{1.5}}} = -0.012083 \cdot \mathrm{TSR}^2 - 0.0082166 \cdot \mathrm{TSR} + 0.0067841$	94.72 %
	$\delta = 45^{\mathrm{o}}$	0.3	$\frac{\mathrm{C_t}}{\mathrm{Re^{0.3}}} = 0.03542 \cdot \mathrm{TSR}^2 - 0.03239 \cdot \mathrm{TSR} + 0.01069$	97.54 %

Table 14.- Correlation equations for prototype rotors.

On the other hand, the results obtained from the power coefficient and torque coefficient of the numerical simulations performed for the prototype rotors are shown in Figs. 15, 16, 18, 19, 21 and 22. These simulations were performed for Reynolds numbers of $1.094 \cdot 10^5$ and $1.364 \cdot 10^5$ (Prototype rotor with $\delta = 0^{\mathrm{o}}$), $1.094 \cdot 10^5$ and $1.419 \cdot 10^5$ (Prototype rotor with $\delta = 22.5^{\mathrm{o}}$), $1.094 \cdot 10^5$ and $1.311 \cdot 10^5$ (Prototype rotor with $\delta = 45^{\mathrm{o}}$); and for rotational speed equal to 13.51 rad/s and 24.82 rad/s (Prototype rotor with $\delta = 0^{\mathrm{o}}$), 14.24 rad/s and 33.93 rad/s (Prototype rotor with $\delta = 22.5^{\mathrm{o}}$), 17.28 rad/s and 30.58 rad/s (Prototype rotor with $\delta = 45^{\mathrm{o}}$); obtained from the experimental analysis.

In Figs 17, 20 and 23, the average contour of the velocity field resulting from the numerical simulations for each prototype rotor is shown. Analyzing the average contour of the velocity field, some vortices and backwater points are generated in the concave regions of the buckets of the rotors for their positions of 60º, 90º and 120º. These vortices and backwater points are of greater intensity, cause low pressure on the concave side and their magnitude decreases as the torsion angle of the rotors buckets δ increases. For the rest of the positions of the prototype rotors analyzed, the vortices or backwater points are of lesser intensity and, as in the case of the vortices and backwater points mentioned at 60º, 90º and 120º angles, their intensity decreases as the torsion angle of the rotors buckets δ increases. In order to model a dynamic numerical analysis, the velocity field for each position of the rotor angle between the 0° and 180° range was captured using 30° rotor angle increments.

The selection of the rotor angle range was performed according to the axisymmetric geometry of the prototype rotors. Finally, in Tables 15, 16, 17, 18, 19 and 20 a comparison is made between the values of the power coefficient and torque coefficient obtained either experimentally by applying the correlation equation $\frac{\mathrm{C_t}}{\mathrm{Re^n}}$, and those obtained by means of the numerical simulations. As shown in the comparative tables, the relative error between the experimental values and the values obtained by the correlation equation $\frac{\mathrm{C_t}}{\mathrm{Re^n}}$ and the numerical simulations do not exceed 3.5%. Therefore, experimental data and numerical data are shown to have supported each other.

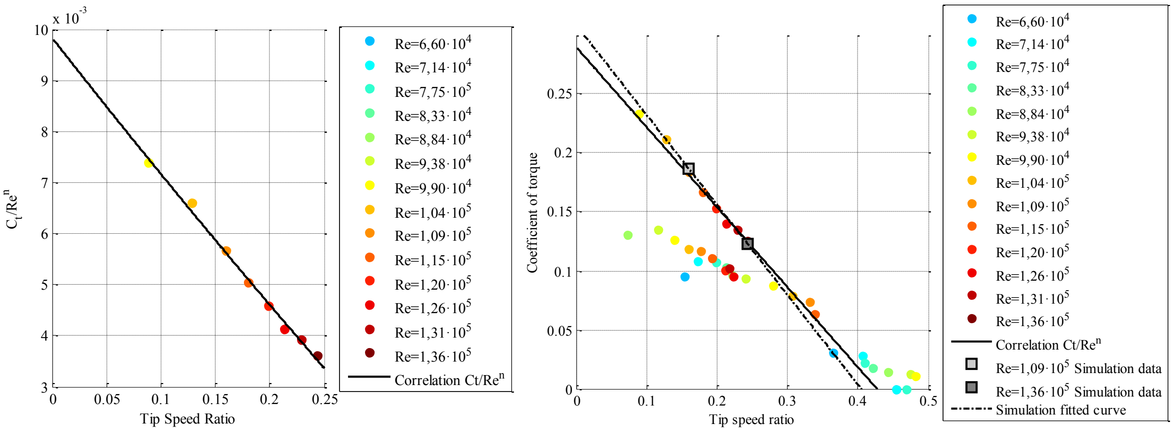

Fig 15.- Ct vs TSR and Correlation Ct/Re^n , and Simulation fitted curve for the prototype rotor δ=0º.

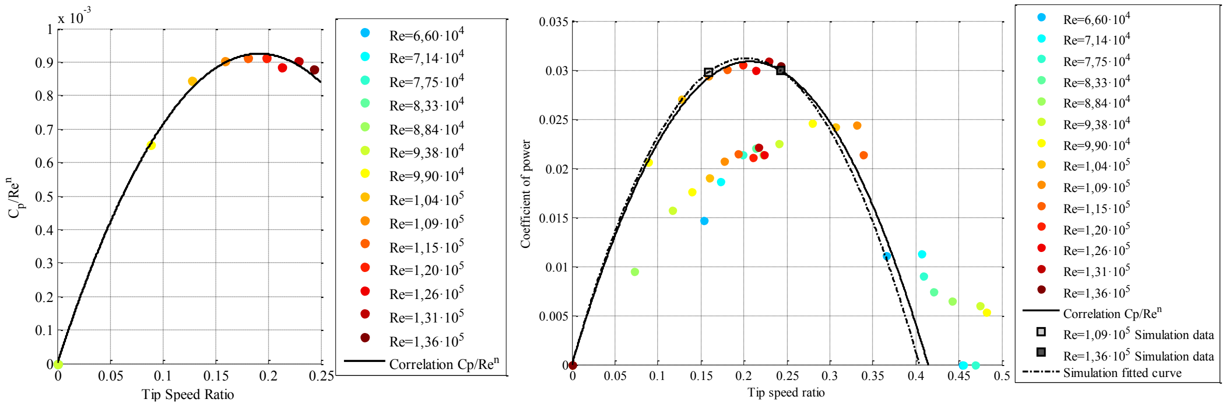

Fig 16.- Cp vs TSR and Correlation Cp/Re^n , and Simulation fitted curve for the prototype rotor δ=0º.

	TSR	$Ct_{experimental}$	$Ct_{simulation}$	$Ct_{correlation}$	$Cp_{experimental}$	$Cp_{simulation}$	$Cp_{correlation}$
Re=1.094·10^5	0.159	0.184	0.187	0.182	0.029	0.030	0.029
Re=1.364·10^5	0.243	0.125	0.123	0.126	0.030	0.030	0.030

Table 15.- Comparison between the results obtained experimentally by means of the correlation equation and the numerical simulation, for the prototype rotor δ = 0º.

	Correlation difference [%]	Simulation difference [%]
Re=1.094·10^5	1.630	1.087
Re=1.364·10^5	1.600	0.800

Table 16.- Error in the approximation of the correlation equation and the numerical simulation for the prototype rotor δ = 0º.

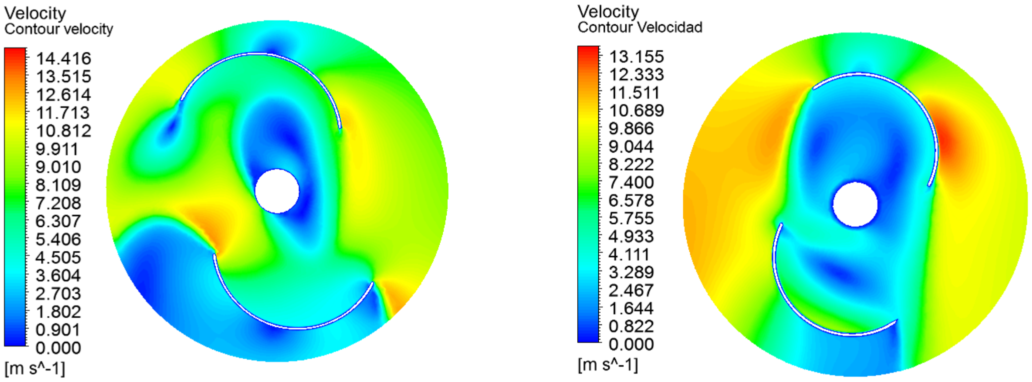

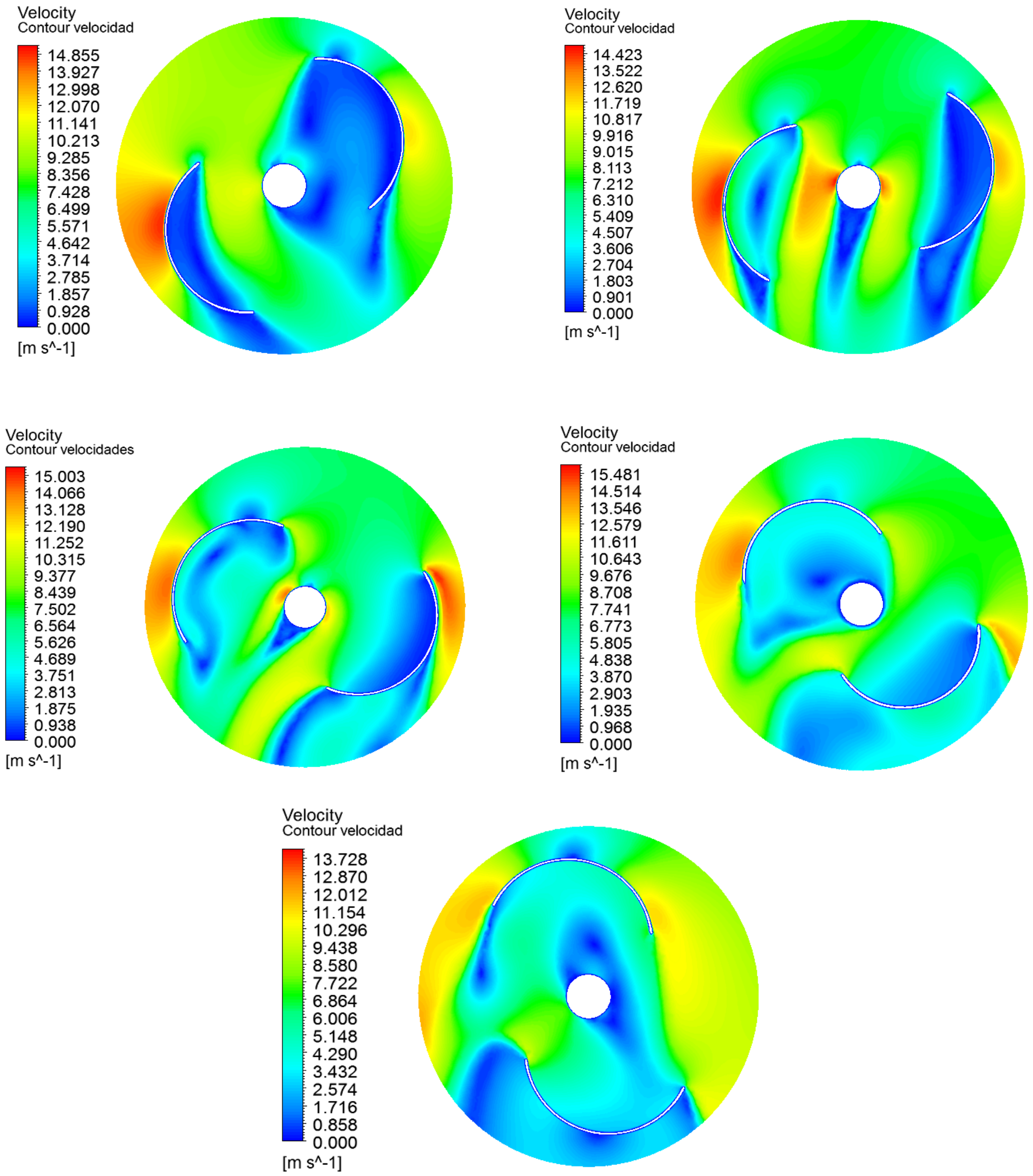

Fig 17.-Velocity map with Reynolds number $1.094\cdot10^5$ for rotor angle 0°, 30°, 60°, 90°, 120°, 150°, 180°. Prototype Rotor δ=0°.

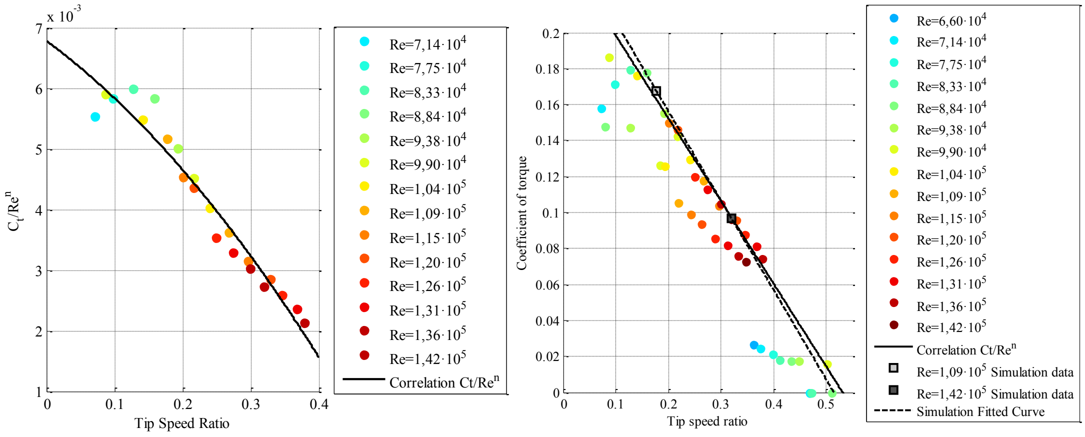

Fig 18.- Ct vs TSR and Correlation Ct/Re^n , and Simulation fitted curve for the prototype rotor δ=22.5°.

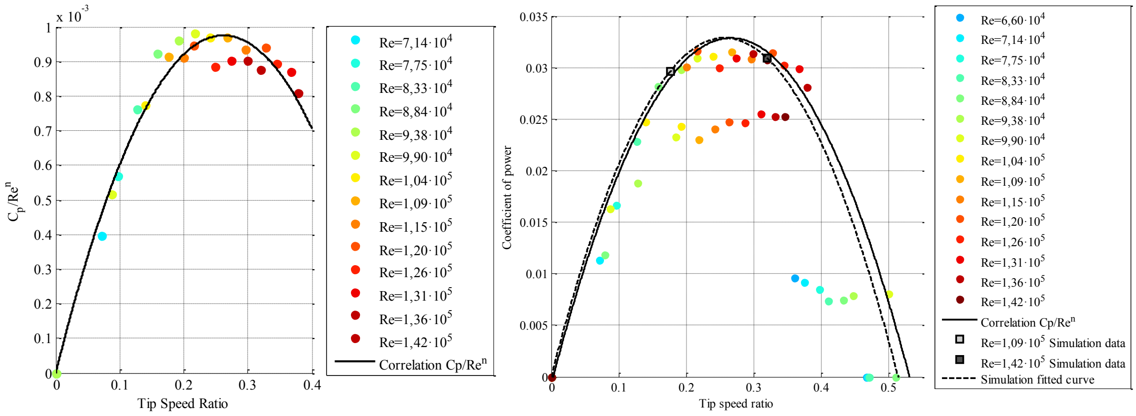

Fig 19.- Cp vs TSR and Correlation Cp/Re^n , and Simulation fitted curve for the prototype rotor δ=22.5º.

	TSR	$C_{t_{\mathrm{experimental}}}$	$C_{t_{\mathrm{simulation}}}$	$C_{t_{\mathrm{correlation}}}$	$C_{p_{\mathrm{experimental}}}$	$C_{p_{\mathrm{simulation}}}$	$C_{p_{\mathrm{correlation}}}$
$Re=1.094\cdot10^5$	0.177	0.168	0.167	0.163	0.030	0.030	0. 30
$Re=1.419\cdot10^5$	0.320	0.096	0.097	0.097	0.030	0.031	0.031

Table 17.- Comparison between the results obtained experimentally by means of the correlation equation and the numerical simulation, for the prototype rotor δ = 22.5º.

	Correlation difference [%]	Simulation difference [%]
$Re=1.094\cdot10^5$	2.976	0.595
$Re=1.364\cdot10^5$	1.042	1.042

Table 18.- Error in the approximation of the correlation equation and the numerical simulation for the prototype rotor δ=22.5º.

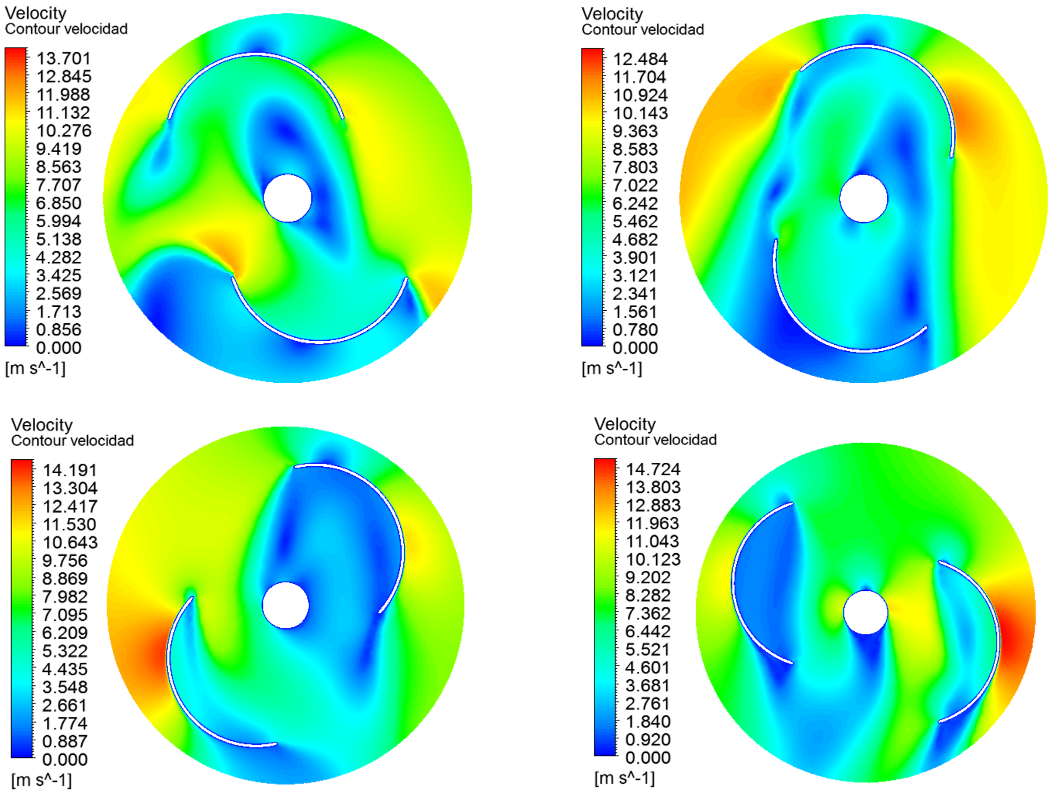

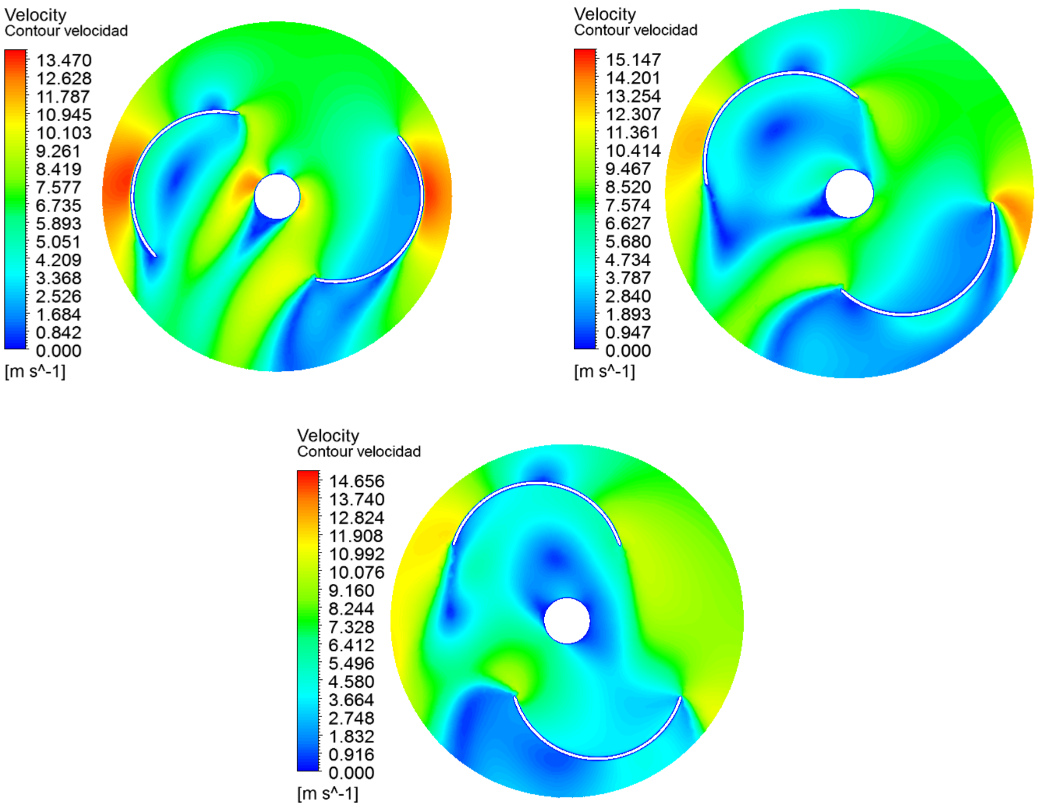

Fig 20.-Velocity map with Reynolds number 1.094·10^5 for rotor angle 0°, 30°, 60°, 90°, 120°, 150°, 180°. Prototype Rotor δ=22.5°.

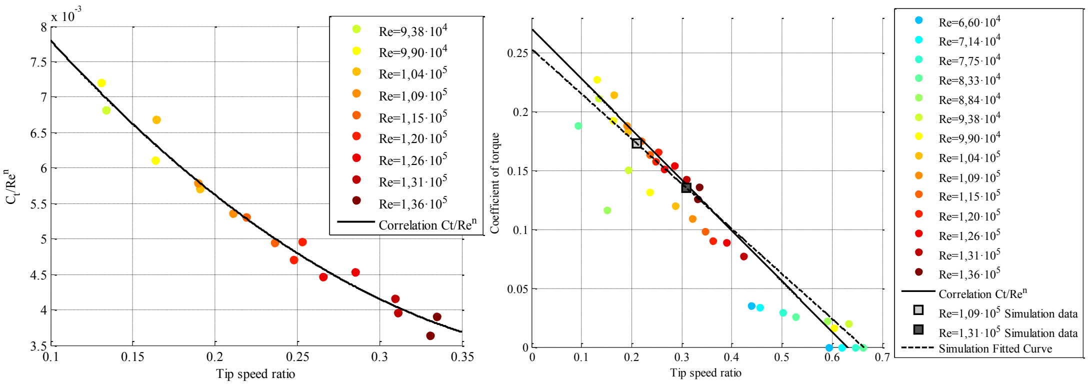

Fig 21.- Ct vs TSR and Correlation Ct/Re^n , and Simulation fitted curve for the prototype rotor δ=45º.

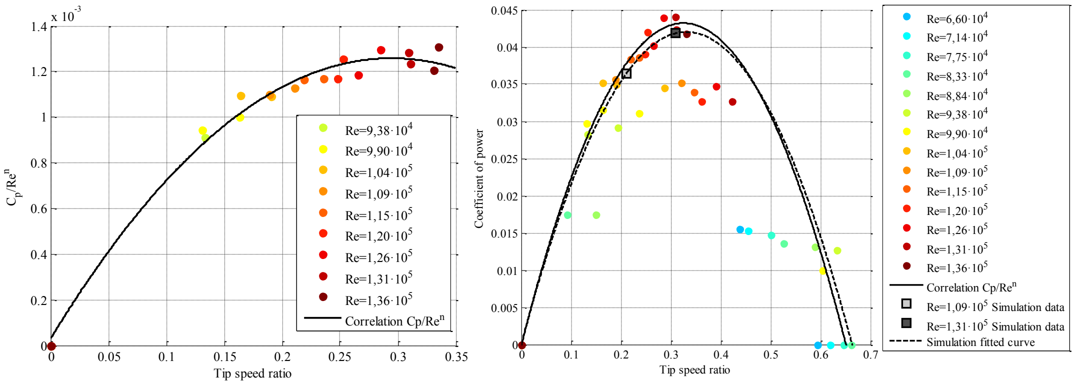

Fig 22.- Cp vs TSR and Correlation Cp/Re^n , and Simulation fitted curve for the prototype rotor δ=45º.

	TSR	$Ct_{experimental}$	$Ct_{simulation}$	$Ct_{correlation}$	$Cp_{experimental}$	$Cp_{simulation}$	$Cp_{correlation}$
$Re=1.094 \cdot 10^5$	0.211	0.174	0.173	0.180	0.037	0.037	0.038
$Re=1.311 \cdot 10^5$	0.309	0.136	0.135	0.138	0.042	0.042	0.043

Table 19.- Comparison between the results obtained experimentally by means of the correlation equation and the numerical simulation, for the prototype rotor δ = 45º.

	Correlation difference [%]	Simulation difference [%]
$Re=1.094 \cdot 10^5$	3.448	0.575
$Re=1.311 \cdot 10^5$	1.471	0.735

Table 20.- Error in the approximation of the correlation equation and the numerical simulation for the prototype rotor δ=45º.

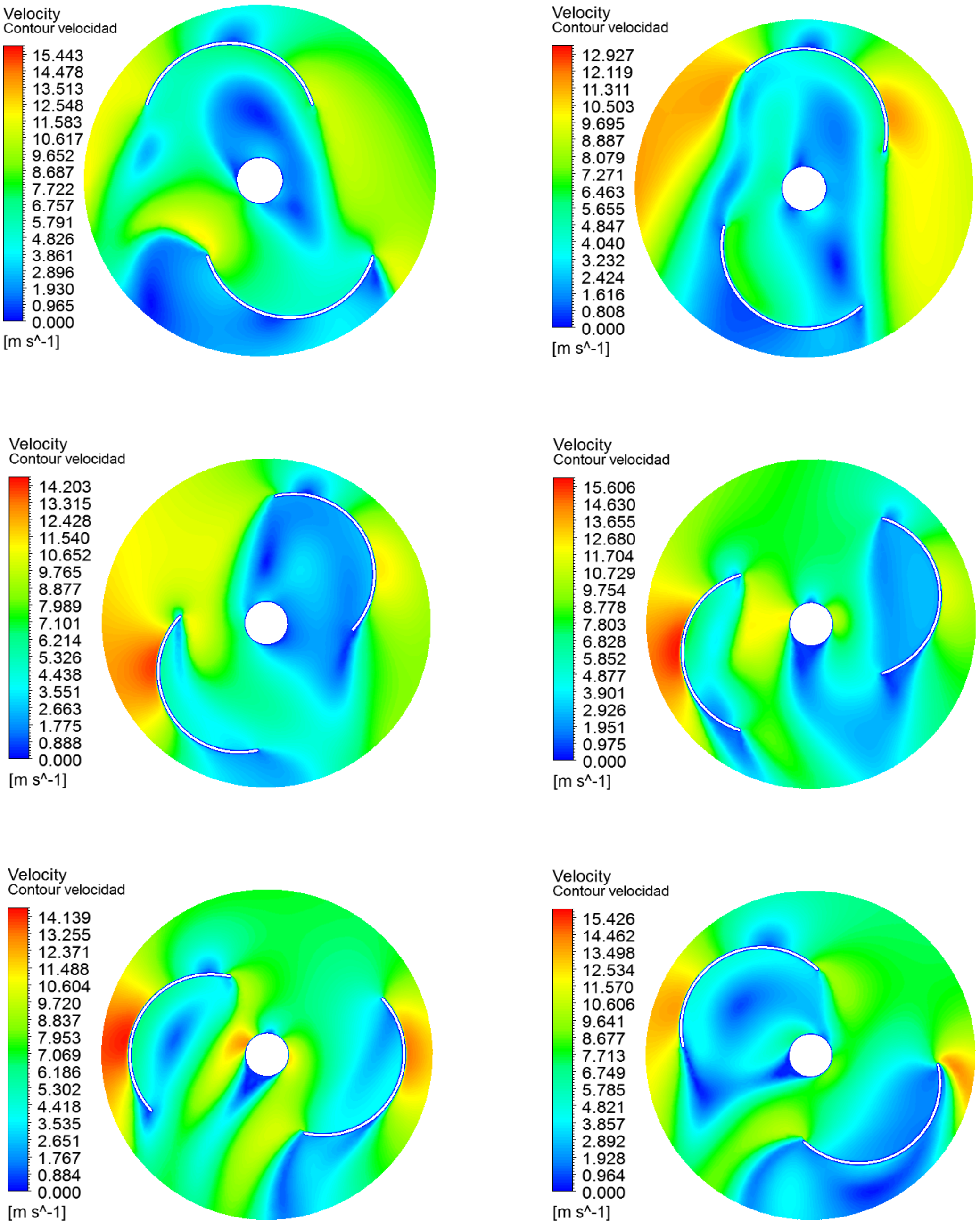

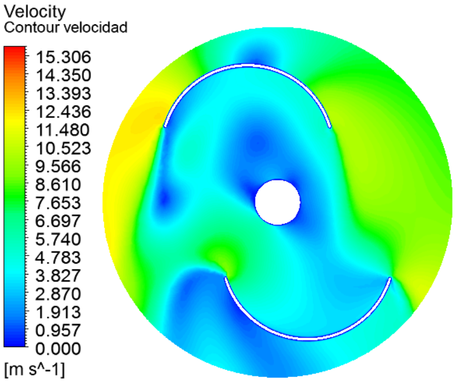

Fig 23.-Velocity map with Reynolds number $1.094\cdot10^5$ for rotor angle 0°, 30°, 60°, 90°, 120°, 150°, 180°. Prototype Rotor δ=45°.

6.4. Comparison between the prototype rotors and the Savonius canonical rotor

Fig 24 shows the superposition of the profiles of the torque coefficient versus rotation angle of the rotor, obtained by means of numerical simulations for the Savonius rotors and prototype canonical rotor for a Reynolds number equal to $7.137\cdot10^4$. These results show the effect of the geometrical parameters on the coefficient of torque and coefficient of power. As can be seen in Table 21, the maximum and minimum torque coefficient for the prototype rotors is obtained for a different rotor angle than for the canonical Savonius rotor. While for prototype rotors the point of maximum torque coefficient is obtained for an angle of rotor 110º-120º ($C_{t_{max}}(\delta = 0^{o})$=0.371, $C_{t_{max}}(\delta = 22.5^{o})$=0.247, $C_{t_{max}}(\delta = 45^{o})$=0.251) for the canonical Savonius rotor the point of maximum coefficient of torque is obtained for a rotor angle of 50 ° ($C_{t_{max}}$=0.872). This indicates that in the prototype rotors the influence of the lift component has a greater effect than the drag component for the force generated by the rotors since the point of maximum torque coefficient is obtained for a rotor angle of 110°- 120°. However, for the canonical Savonius rotor the drag component has greater influence than the lift component for the force generated by the rotor, because the point of maximum torque coefficient is obtained for a rotor angle of 50°.

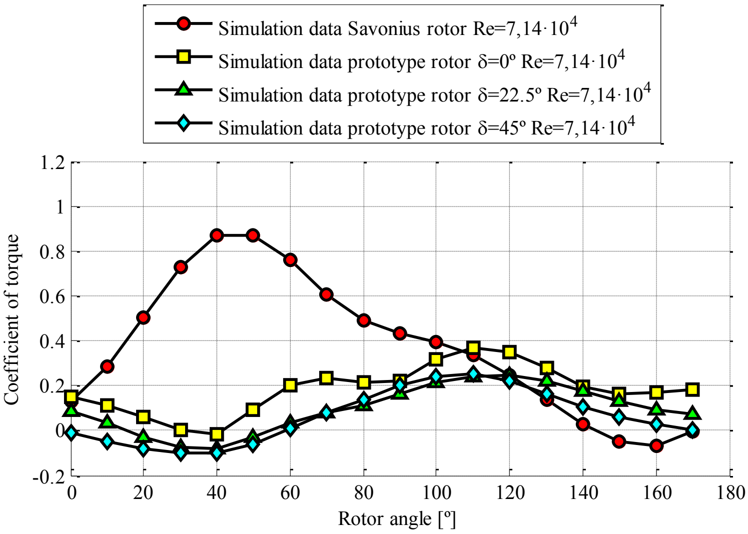

Fig 24.- Comparison of Ct vs Rotor angle at a Reynolds number $7.137\cdot10^4$ for the prototype rotors and the canonical Savonius rotor.

Re=$7.137\cdot10^4$	Savonius rotor	Prototype rotors		
		$\delta = 0^{o}$	$\delta = 22.5^{o}$	$\delta = 45^{o}$
$C_{t_{max}}$	0.872	0.371	0.247	0.251
$C_{t_{min}}$	-0.065	-0.015	-0.082	-0.098
Location of $C_{t_{max}}$ [º]	50º	110º	120º	110º
Location of $C_{t_{min}}$ [º]	160º	40º	40º	40º

Table 21.- Maximum torque coefficient versus rotor angle at a Reynolds number $7,137\cdot10^4$ for the prototype rotors and the canonical Savonius rotor.

Fig 25 shows a comparison of the coefficient of torque and power coefficient between the prototype rotors and the canonical Savonius rotor for a Reynolds number equal to $7.137 \cdot 10^4$. Table 22 collects the magnitude of the maximum values for each coefficient of torque and power curve for the prototype rotors and the Savonius canonical rotor. These results show that the canonical Savonius rotor generates greater torque and power than prototype rotors at a higher tip speed ratio. This is due to the difference in speed of rotation between the prototype rotors and the Savonius canonical rotor. Whereas in the prototype rotors the maximum coefficient of torque and power is obtained for a tip speed ratio of 0.173, 0.072 and 0.455, respectively, For the Savonius canonical rotor the maximum coefficient of torque and power is obtained for a tip speed ratio of 0.712. That is to say, in order to obtain a coefficient of torque and power analogous to that of the canonical Savonius rotor, the prototype rotors must act with a higher Reynolds number.

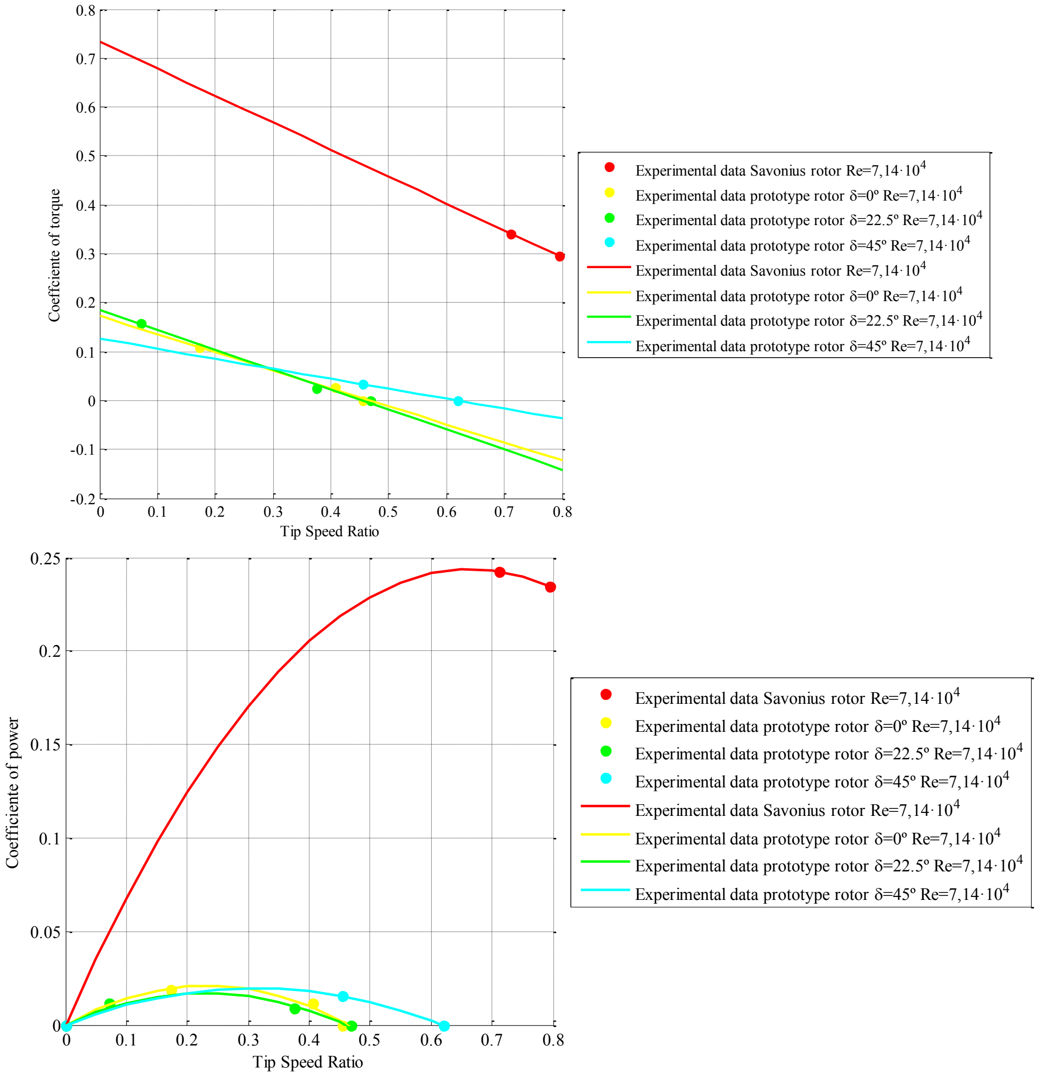

Fig 25.- Comparison of Ct vs TSR and Cp vs TSR to a Reynolds number $7.137 \cdot 10^4$ for the prototype rotors and the canonical Savonius rotor.

Re=$7.137 \cdot 10^4$		$C_{t_{max}}$	$C_{p_{max}}$	TSR at $C_{p_{max}}$, $C_{t_{max}}$
Prototype Rotors	$\delta = 0^o$	0.108	0.019	0.173
	$\delta = 22.5^o$	0.158	0.011	0.072
	$\delta = 45^o$	0.034	0.015	0.455
Savonius rotor		0.341	0.243	0.712

Table 22.- Coefficient of torque and coefficient of power with maximum tip speed ratio at a number of Reynolds $7.137 \cdot 10^4$ for prototype rotors and Savonius rotor.

Finally, table 22 shows the maximum power coefficient values of the prototype rotors, as well as the tip speed ratio and the Reyndols number corresponding to these maximum values. These maximum power coefficients were compared with the power coefficients obtained in the canonical Savonius rotor for the tip speed ratio of the maximum prototypes rotor power coefficient. These results show an approximate reduction of 49-55% of the power coefficient in the prototype rotors versus the canonical Savonius rotor. In addition, it is verified that as the angle of rotation or torsion δ of the prototype rotors improves the behavior of the prototype rotor and increases the coefficient of torque, power coefficient and mechanical power obtained.

Prototype rotors	$C_{p_{max}}$	Corresponding Reynolds number	TSR at $C_{p_{max}}$	Savonius C_p at TSR of the maximum rotor power coefficient	C_t, C_p difference [%]
$\delta = 0°$	0.031	$1.36 \cdot 10^5$	0.229	0.070	55.714
$\delta = 22.5°$	0.032	$1.20 \cdot 10^5$	0.217	0.0670	52.239
$\delta = 45°$	0.046	$1.36 \cdot 10^5$	0.335	0.091	49.451

Table 23.- Comparison of maximum power coefficients for prototype rotors and power coefficients for the Savonius rotor a tip speed ratio of the maximum prototypes rotor power coefficient.

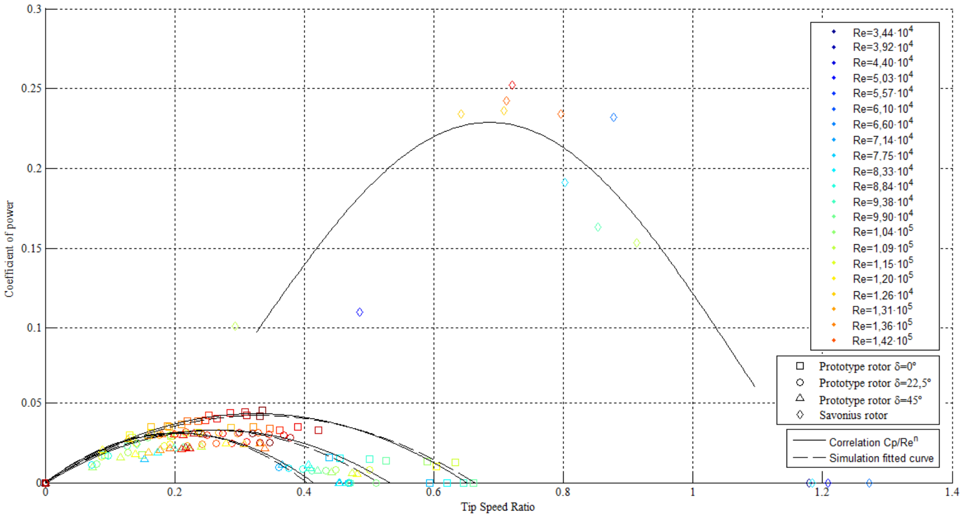

Fig 26 .- Comparison of Cp vs TSR at a Reynolds number between $3.436 \cdot 10^4$ and $1.419 \cdot 10^5$ for the prototype rotors and the canonical Savonius rotor. Results obtained experimentally and by means of the correlation equation.

7. Conclusions

This paper presents the numerical-experimental study of a new rotor, adapted from a conventional Savonius rotor, to which aesthetic, ergonomic and functional requirements have been incorporated, allowing it to form an integral part of sustainable consumer products. Both studies aim to evaluate the performance of the new rotor. A set of translational, rotational and scale symmetry operations was applied to the bucket sections of a canonical Savonius rotor in order to transform the base cylindrical surfaces into organic type surfaces easily integrated into the product environment. The rotor has been designed in parametric format allowing it to adapt automatically to different products by simply changing its dimensions.

In order to validate the performance of the rotor, this was applied to a patented consumer product integrated into its geometry. The reduced dimensions of the device in which it was integrated and its requirement of lateral accessibility to the inside shaft of the rotor enabled the performance of the rotor to be obtained in design conditions outside the optimum range of the technical parameters of the rotor. The modified Savonius rotor has been compared to a conventional Savonius rotor with the same aspect ratio in terms of power coefficient, torque coefficient and mechanical power generated.

The new rotor was tested in an open jet wind tunnel in order to verify the level of influence of product design parameters on rotor performance. Experiments were carried out for Reynolds values included in the range of [$3.436 \cdot 10^4$ y $1.419 \cdot 10^5$]. The experimental results have been validated with a numerical analysis using an incompressible unsteady Reynolds average Navier-Stokes model, obtaining a deviation of 3.5% between the experimental results and those obtained numerically. For the range of tip speed ratio values between 0.223 and 0.335, the rotor fulfills the functional requirements of the product of small-scale power generation, although in view of the results an increase in the speed of operation analyzed previously in the paper would be favorable.

The set of symmetry and translation operations performed on the canonical Savonius rotor greatly influences the design parameters of the rotor β_x and β_y, increasing its value and affecting its performance. This can be improved in those designs where a large value of lateral accessibility is not required, decreasing the value of the parameters β_x and β_y and which would favorably influence the performance of the rotor. Introducing the golden ratio in the dimensioning of the rotor greatly improves the harmonic proportions of the product, making it better integrated into the environment. The scaling process of the sections causes the value of β_y to be variable along the height of the rotor, decreasing by 61.80% from the central sections to the ends. The aspect ratio AR for the new rotor has a value of 1.608, equal to the golden number, being within the range of recommended values for good technical performance.

The behavior of the rotors with different rotation angles in the sections of their buckets has been analyzed, observing that as the value of the rotation angle δ increases, the speed of the rotor increases, improving the power coefficient and the tip speed ratio, as well as the mechanical power generated. For a rotation angle δ of 45°, the power coefficient values improve by 32% compared to the values obtained for the angle 0°. The experimental and numerical analyses performed on the new rotor show a lower speed ratio compared to that of the conventional Savonius rotor. This indicates that the rotation speed of the new rotor is lower than the Savonius rotor, as it is shown that the Reynolds numbers at which the experimental tests of the new rotor have been performed are higher than in the Savonius rotor. This fact indicates a more favorable operation for the new rotor within a range of wind speeds superior to the range of the Savonius.

The new rotor is born as a suitable variant of the Savonius rotor for small-scale energy applications, or to reduce the energy consumption of products where aesthetic and ergonomic requirements are necessary for sale. The new rotor maintains the advantages of the Savonius rotor at the same time that it integrates perfectly into the geometry of the product, giving it personality and making it desirable for consumers. The new rotor is part of a new line of research consisting of incorporating technical elements capable of contributing to the energy generation of the product, fulfilling its own requirements of aesthetic and ergonomic design with the aim of improving the urban sustainability of society.

8. Nomenclature

Nomenclature			
$\mathcal{S}$	Canonical Savonius rotor	C_t	Coefficient of torque
$\mathcal{B}_{\mathcal{S}}$	Buckets of the rotor $\mathcal{S}$	D	Rotor diameter [m]
$\mathcal{P}_j$	New rotor adapted from $\mathcal{S}$	R_s	Bucket Ratius [m]
$\mathcal{B}_{\mathcal{P}j}$	Buckets of the $\mathcal{P}_j$ rotor	H	Rotor height [m]
j	Number of prototype rotors; in the present paper the value of j=3	ϕ	Golden number
Π_i	Set of cutting-planes of the rotor buckets, parallel to the XY plane	ℓ_w	Distance from downstream rotors
r_{s1i}, r_{s2i}	Buckets sections of the rotor $\mathcal{S}$	H_{wt}	Wind tunnel height [m]
$r_{\mathcal{P}j1i}$, $r_{\mathcal{P}j2i}$	Buckets sections of the rotor $\mathcal{P}_j$	W_{wt}	Wind tunnel width [m]
H_s	Height of the rotor $\mathcal{S}$ [m]	B	Blockage ratio
H_p	Height of the rotor $\mathcal{P}_j$ [m]	l	Distance between the rotor axis and the application point of the force [m]
H	Generic height of the rotor [m]	T	Torque [N·m]
δ	Torsion angle of the rotors buckets [º]	T_s	Static Torque [N·m]
A_R	Aspect ratio	F_{din}	Force applied by the rotor [N]
e_{p_x}	Overlap distance on the X axis for $\mathcal{P}_j$ [m]	TSR	Tip speed ratio
e_{p_y}	Overlap distance on the Y axis for $\mathcal{P}_j$ [m]	U_∞	Free stream wind velocity [m/s]
e_x	Overlap distance on the axis X for $\mathcal{S}$[m]	ω	Rotor angular velocity [rad/s]
$\mathcal{A}$	Internal element to the rotor	ρ	Density of air [kg/m^3]
a_{shaft}	Diameter of the internal element to the rotor [m]	μ	Viscosity of air [Pa·s]
β_x	Overlap ratio on the X axis	L_w	Length of the wind tunnel [m]
β_y	Spacing ratio on the Y axis	θ	Rotor angle [º]
C_p	Coefficient of power		

Table 24.- Nomenclature used in the present paper.

Acknowledgments

This work has been supported by the University of Jaen through the project titled ” Diseño de un bastón ecológico de senderismo generador eólico hidraulico” Project Code (AC20/2015-12) and (R1 A7/2017). The authors would like to thank the Mechanical Engineering Department at Jaen University for using the wind tunnel to achieve the experimental study. The authors would like to thank the reviewers for comments that improved the exposition.

9. Bibliography

[1] Marinić-Kragić, I., Vučina, D., & Milas, Z. (2018). Numerical workflow for 3D shape optimization and synthesis of vertical-axis wind turbines for specified operating regimes. Renewable Energy, 115, 113-127.

[2] Roy, S., & Saha, U. K. (2014). An adapted blockage factor correlation approach in wind tunnel experiments of a Savonius-style wind turbine. Energy Conversion and Management, 86, 418-427.

[3] Al-Hadhrami, L. M. (2014). Performance evaluation of small wind turbines for off grid applications in Saudi Arabia. Energy Conversion and Management, 81, 19-29.

[4] Bangga, G., Lutz, T., Jost, E., & Krämer, E. (2017). CFD studies on rotational augmentation at the inboard sections of a 10 MW wind turbine rotor. Journal of Renewable and Sustainable Energy, 9(2), 023304.

[5] Mereu, R., Federici, D., Ferrari, G., Schito, P., & Inzoli, F. (2017). Parametric numerical study of Savonius wind turbine interaction in a linear array. Renewable Energy, 113, 1320-1332.

[6] Roy, S., Das, R., & Saha, U. K. (2018). An inverse method for optimization of geometric parameters of a Savonius-style wind turbine. Energy Conversion and Management, 155, 116-127.

[7] Ducoin, A., Shadloo, M. S., & Roy, S. (2017). Direct Numerical Simulation of flow instabilities over Savonius style wind turbine blades. Renewable Energy, 105, 374-385.

[8] Goodarzi, M., & Keimanesh, R. (2015). Numerical analysis on overall performance of Savonius turbines adjacent to a natural draft cooling tower. Energy Conversion and Management, 99, 41-49

[9] Saha, U. K., & Rajkumar, M. J. (2006). On the performance analysis of Savonius rotor with twisted buckets. Renewable energy, 31(11), 1776-1788.

[10] Roy, S., & Saha, U. K. (2015). Wind tunnel experiments of a newly developed two-bucketd Savonius-style wind turbine. Applied Energy, 137, 117-125.

[11] Kamoji, M. A., Kedare, S. B., & Prabhu, S. V. (2009). Experimental investigations on single stage modified Savonius rotor. Applied Energy, 86(7), 1064-1073.

[12] Roy, S., & Ducoin, A. (2016). Unsteady analysis on the instantaneous forces and moment arms acting on a novel Savonius-style wind turbine. Energy Conversion and Management, 121, 281-296.

[13] Tian, W., Mao, Z., Zhang, B., & Li, Y. (2017). Shape Optimization of a Savonius Wind Rotor with Different Convex and Concave Sides. Renewable Energy.

[14] Lee, J. H., Lee, Y. T., & Lim, H. C. (2016). Effect of twist angle on the performance of Savonius wind turbine. Renewable Energy, 89, 231-244.

[15] Damak, A., Driss, Z., & Abid, M. S. (2013). Experimental investigation of helical Savonius rotor with a twist of 180. Renewable Energy, 52, 136-142.

[16]Yang H.B. Wind Tunnel study on the performance characteristics of SAvonius Wind Turbine [Master Thesis]Pusan National University 2013

[17] Al-Kayiem, H. H., Bhayo, B. A., & Assadi, M. (2016). Comparative critique on the design parameters and their effect on the performance of S-rotors. Renewable Energy, 99, 1306-1317.

[18] Roy, S., & Saha, U. K. (2013). Review of experimental investigations into the design, performance and optimization of the Savonius rotor. Proceedings of the Institution of Mechanical Engineers, Part A: Journal of Power and Energy, 227(4), 528-542.

[19] Blackwell, B. F., Sheldahl, R. F., & Feltz, L. V. (1977). Wind tunnel performance data for two-and three-bucket Savonius rotors. Albuquerque, NM: Sandia Laboratories.

[20] Saha, U. K., Thotla, S., & Maity, D. (2008). Optimum design configuration of Savonius rotor through wind tunnel experiments. Journal of Wind Engineering and Industrial Aerodynamics, 96(8), 1359-1375.

[21] Akwa, J. V., da Silva Júnior, G. A., & Petry, A. P. (2012). Discussion on the verification of the overlap ratio influence on performance coefficients of a Savonius wind rotor using computational fluid dynamics. Renewable energy, 38(1), 141-149.

[22] Fujisawa, N. (1992). On the torque mechanism of Savonius rotors. Journal of Wind Engineering and Industrial Aerodynamics, 40(3), 277-292.

[23] Ushiyama, I., & Nagai, H. (1988). Optimum design configurations and performance of Savonius rotors. Wind Engineering, 59-75.

[24] Jian, C., Kumbernuss, J., Linhua, Z., Lin, L., & Hongxing, Y. (2012). Influence of phase-shift and overlap ratio on Savonius wind turbine’s performance. Journal of Solar Energy Engineering, 134(1) 1-9.

[25] Saha, U. K., Thotla, S., & Maity, D. (2008). Optimum design configuration of Savonius rotor through wind tunnel experiments. Journal of Wind Engineering and Industrial Aerodynamics, 96(8), 1359-1375.

[26] Ali, M. H. (2013). Experimental comparison study for Savonius wind turbine of two & three buckets at low wind speed. International Journal of Modern Engineering Research (IJMER), 3(5), 2978-2986.

[27] Mahmoud, N. H., El-Haroun, A. A., Wahba, E., & Nasef, M. H. (2012). An experimental study on improvement of Savonius rotor performance. Alexandria Engineering Journal, 51(1), 19-25.

[28] Hayashi, T., Yan, L. I., & Yutaka, H. A. R. A. (2005). Wind tunnel tests on a different phase three-stage Savonius rotor. JSME International Journal Series B Fluids and Thermal Engineering, 48(1), 9-16.

[29] Menet, J. L. (2004). A double-step Savonius rotor for local production of electricity: a design study. Renewable energy, 29(11), 1843-1862.

[30] Altan, B. D., & Atılgan, M. (2010). The use of a curtain design to increase the performance level of a Savonius wind rotors. Renewable Energy, 35(4), 821-829.

[31] Altan, B. D., Altan, G., & Kovan, V. (2016). Investigation of 3D printed Savonius rotor performance. Renewable Energy, 99, 584-591.

[32] Mohamed, M. H., Janiga, G., Pap, E., & Thévenin, D. (2010). Optimization of Savonius turbines using an obstacle shielding the returning bucket. Renewable Energy, 35(11), 2618-2626.

[33] Sharma, S., & Sharma, R. K. (2016). Performance improvement of Savonius rotor using multiple quarter blades– A CFD investigation. Energy Conversion and Management, 127, 43-54.

[34] Sharma, S., & Sharma, R. K. (2017). CFD investigation to quantify the effect of layered multiple miniature blades on the performance of Savonius rotor. Energy Conversion and Management, 144, 275-285.

[35] Korprasertsak, N., & Leephakpreeda, T. (2016). Analysis and optimal design of wind boosters for Vertical Axis Wind Turbines at low wind speed. Journal of Wind Engineering and Industrial Aerodynamics, 159, 9-18.

[36] Alexander, A. J., & Holownia, B. P. (1978). Wind tunnel tests on a Savonius rotor. Journal of Wind Engineering and Industrial Aerodynamics, 3(4), 343-351.

[37] Krause, C. L. (2001). Our visual landscape: Managing the landscape under special consideration of visual aspects. Landscape and Urban planning, 54(1), 239-254.

[38] Chong, W. T., Pan, K. C., Poh, S. C., Fazlizan, A., Oon, C. S., Badarudin, A., & Nik-Ghazali, N. (2013). Performance investigation of a power augmented vertical axis wind turbine for urban high-rise application. Renewable Energy, 51, 388-397

[39] Müller, G., Chavushoglu, M., Kerri, M., & Tsuzaki, T. (2017). A resistance type vertical axis wind turbine for building integration. Renewable Energy, 111, 803-814.

[40] Orlandi, A., Collu, M., Zanforlin, S., & Shires, A. (2015). 3D URANS analysis of a vertical axis wind turbine in skewed flows. Journal of Wind Engineering and Industrial Aerodynamics, 147, 77-84

[41] Bangga, G., Lutz, T., Dessoky, A., & Krämer, E. (2017). Unsteady Navier-Stokes studies on loads, wake, and dynamic stall characteristics of a two-bladed vertical axis wind turbine. Journal of Renewable and Sustainable Energy, 9(5), 053303.

[42] Ferrari, G., Federici, D., Schito, P., Inzoli, F., & Mereu, R. (2017). CFD study of Savonius wind turbine: 3D model validation and parametric analysis. Renewable Energy, 105, 722-734.

[43] Bhuyan, S., & Biswas, A. (2014). Investigations on self-starting and performance characteristics of simple H and hybrid H-Savonius vertical axis wind rotors. Energy Conversion and Management, 87, 859-867.

[44] Simões, T., & Estanqueiro, A. (2016). A new methodology for urban wind resource assessment. Renewable Energy, 89, 598-605.

[45] Lockwood, T. (2010). Design thinking: Integrating innovation, customer experience, and brand value. Skyhorse Publishing, Inc.

[46] Karlsson, R., & Luttropp, C. (2006). EcoDesign: what's happening? An overview of the subject area of EcoDesign and of the papers in this special issue. Journal of cleaner production, 14(15), 1291-1298.

[47]Walker James(2016). Golden Ratio axial flow apparatus. Patent Number US9328717

[48] Choy Nam Hyun(2016) A rotor for wind power generator. Patent Number KR101590054

[49] https://enessere.com/it/hercules/hercules-wind-turbine/

[50] http://enessere.com/en/enessere-won-the-focus-open-silver-design-award-in-germany/

[51] http://www.newwind.fr/

[52] Benyus, J. M. (1997). Biomimicry (p. 1). New York: William Morrow

[53] http://leviathanenergy.com/technology/wind-tulips/

[54] Lidwell, W., Holden, K., & Butler, J. (2010). Universal principles of design, revised and updated: 125 ways to enhance usability, influence perception, increase appeal, make better design decisions, and teach through design. Rockport Pub.

[55] Martin-Doñate Cristina; Rubio-Paramio Miguel Angel; Mercado-Colmenero Jorge Manuel; Rus Casas Catalina (2017) Bastón electrónico de senderismo. ES2598296B2

[56]http://www.lavanguardia.com/tecnologia/20170717/424184267868/patentan-un-baston-de-senderismo-que-permite-recargar-dispositivos-moviles.html

[57] Tilley, A. (1993). The measure of man and woman: human factors in design.

[58] http://www.ansys.com/es

[59] http://www.solidworks.es

[60] Burçin Deda Altan , Mehmet Atılgan (2008). An experimental and numerical study on the improvement of the performance of Savonius wind rotor. Energy Conversion and Management 49 (2008) 3425–3432.

[61] Robert – Howell, Ning Qin, Jonathan Edwards, Naveed Durrani (2010). Wind tunnel and numerical study of a small vertical axis wind turbine. Renewable Energy 35 (2010) 412-422.

[62] Wenlong Tian, Baowei Song, James H. VanZwieten, Parakram Pyakurel (2015). Computational Fluid Dynamics Prediction of a Modified Savonius Wind Turbine with Novel Blade Shapes. Energies 8 (2015) 7915-7929.

[63] Krzysztof Rogowski, Ryszard Maronski (2015). CFD computation of the Savonius Rotor. Journal of Theoretical and Applied Mechanics 53 (2015) 37-45.

[64] Burcin Deda Altan , Gurkan Altan, Volkan Kovan (2016). Investigation of 3D printed Savonius rotor performance. Renewable Energy 99 (2016) 584-591.

[65] ANSYS FLUENT Theory Guide. http://ansys.com

[66] Bangga, G,. Thorsten, L., & Kramer, E. (2017). Root flow characteristics and 3D effects of an isolated wind turbine rotor. Journal of Mechanical Science and Technology, 31 (8), 3839-3844.

Vitae

Jorge Manuel Mercado Colmenero received his B.Eng and M.Eng. in Mechanical Engineering in 2012 and 2014 respectivily from the University of Jaén in Spain. In 2014 he joined the Design, Engineering Graphics and Project departament at Jaen university as a PhD student. He is currently developing his thesis about automatic analyses and design of injection plastic mold, including demoldability, ejection system, cooling system design and CAD-CAE design and manufacturing.

Dr. Miguel Angel Rubio Paramio received his MEng and Ph.D in Mechanical Engineering in 1992 and 2000 respectively from Polytechnic University of Madrid in Spain. In 1994 he joined the University of Jaen and currently he teaches courses of Computer-aided Design, Manufacturing and Engineering in the Engineering Graphics, Design and Projects Department. His thesis was focused on automatic analysis of injection plastic part. His research interests include CAD-CAM-CAE, Design for Manufacturing, computational geometry, constraint-based parametric modeling, and their applications on plastic injection mold design and manufacturing.

Francisca Guerrero-Villar received his B.Eng and M.Eng. in Mechanical Engineering from the University of Sevilla in Spain She worked for several years (2007-2013) as top head of the Technological Center CETEMET. She has been main researcher in two INNTERCONECTA call grant competitive projects (SEAMAR, ODISEO), and in a INNPACTO call grant competitive project (INNVEXTRAN).Since 2014 until now is a researcher at the Jaen University specialized in renewable energy.

Dr. Cristina Martín Doñate received her B.Eng. and M.Eng. in Electrical - Electronics Engineering and Industrial Engineering (Polytechnic University of Valencia - Spain) in 1997 and Ph.D in Industrial Engineering (University of Jaen - Spain) in 2010. She worked for several years as project manager on developing new products in automotive manufacturing industries. She developed research at the Technical University of Graz in Austria, and at the University of Applied sciences of Rosenheim in Germany in the field of manufacturing systems. She is currently Professor at Jaen University where she develops research and conduct research projects in manufacturing systems, plastic injection mold design and technology, CAD systems and new products development.